

Simultaneous X-ray and radio observations of the radio-mode-switching pulsar PSR B1822–09

W. Hermsen,^{1,2★} L. Kuiper,¹ J. W. T. Hessels,^{2,3★} D. Mitra,^{4,5,8★} J. M. Rankin,^{2,5}
B. W. Stappers,⁶ G. A. E. Wright,^{6,7} R. Basu,^{4,8} A. Szary^{3,8} and J. van Leeuwen^{2,3}

¹*SRON Netherlands Institute for Space Research, Sorbonnelaan 2, NL-3584 CA Utrecht, the Netherlands*

²*Anton Pannekoek Institute for Astronomy, University of Amsterdam, Science Park 904, NL-1098 XH Amsterdam, the Netherlands*

³*ASTRON, the Netherlands Institute for Radio Astronomy, Postbus 2, NL-7990 AA Dwingeloo, the Netherlands*

⁴*National Centre for Radio Astrophysics (NCFRA-TIFR), Post Bag 3, Ganeshkhind, Pune University Campus, Pune 411007, India*

⁵*Physics Department, University of Vermont, Burlington, VT 05405, USA*

⁶*Jodrell Bank Centre for Astrophysics, School of Physics and Astronomy, University of Manchester, Manchester M13 9PL, UK*

⁷*Astronomy Centre, University of Sussex, Falmer, Brighton BN1 9QJ, UK*

⁸*Janusz Gil Institute of Astronomy, University of Zielona Góra, Lubuska 2, PL-65-265 Zielona Góra, Poland*

Accepted 2016 November 29. Received 2016 November 17; in original form 2016 September 13

ABSTRACT

We report on simultaneous X-ray and radio observations of the radio-mode-switching pulsar PSR B1822–09 with ESA’s *XMM–Newton* and the Westerbork Synthesis Radio Telescope, Giant Metrewave Radio Telescope and Lovell radio telescopes. PSR B1822–09 switches between a radio-bright and radio-quiet mode, and we discovered a relationship between the durations of its modes and a known underlying radio-modulation time-scale within the modes. We discovered X-ray (energies 0.2–1.4 keV) pulsations with a broad sinusoidal pulse, slightly lagging the radio main pulse in phase by 0.094 ± 0.017 , with an energy-dependent pulsed fraction varying from ~ 0.15 at 0.3 keV to ~ 0.6 at 1 keV. No evidence is found for simultaneous X-ray and radio mode switching. The total X-ray spectrum consists of a cool component ($T \sim 0.96 \times 10^6$ K, hotspot radius $R \sim 2.0$ km) and a hot component ($T \sim 2.2 \times 10^6$ K, $R \sim 100$ m). The hot component can be ascribed to the pulsed emission and the cool component to the unpulsed emission. The high-energy characteristics of PSR B1822–09 resemble those of middle-aged pulsars such as PSR B0656+14, PSR B1055–52 and Geminga, including an indication for pulsed high-energy gamma-ray emission in *Fermi* Large Area Telescope data. Explanations for the high pulsed fraction seem to require different temperatures at the two poles of this orthogonal rotator, or magnetic anisotropic beaming effects in its strong magnetic field. In our X-ray skymap, we found a harder source at only 5.1 ± 0.5 arcsec from PSR B1822–09, which might be a pulsar wind nebula.

Key words: stars: neutron–pulsars: general–radio continuum: stars–X-rays: individual: PSR B1822–09.

1 INTRODUCTION

In this paper, we present the results of simultaneous X-ray and radio observations of the radio-mode-switching pulsar PSR B1822–09.

The project was stimulated by the success of an earlier similar campaign involving the mode-switching pulsar PSR B0943+10, which resulted in the discovery of synchronous mode switching in the pulsar’s radio and X-ray emission properties (Hermsen et al. 2013). This was then followed up by a more extended campaign (Mereghetti et al. 2016) in which the synchronous mode switching of PSR B0943+10 was confirmed and which enabled its nature

to be better established, discovering that both pulsed and unpulsed X-ray emission are present in both modes but at differing levels and that these properties may evolve during one of the modes.

These completely unexpected results are of great importance for the understanding of the physical processes in pulsar magnetospheres. In addition, separate investigations have challenged the earlier perception that radio-mode switching is a detail of polar cap and/or magnetospheric physics by the identification of a relationship between the spin properties of neutron stars and their radio emission modes (Kramer et al. 2006; Lyne et al. 2010; Camilo et al. 2012; Lorimer et al. 2012). The implication of these results is that mode switching is due to an inherent, perhaps universal, pulsar process that causes a sudden change in the rate of angular momentum loss that is communicated along the open field lines of

* E-mail: w.hermsen@sron.nl (WH); J.W.T.Hessels@uva.nl (JWTH); dmitra@ncra.tifr.res.in (DM)

the magnetosphere. This link with the rapid switching observed in radio emission modes suggests a transformation of the global magnetospheric state in less than a rotation period. Nevertheless, the two X-ray radio campaigns on PSR B0943+10 have yet to conclusively answer the fundamental question as to whether the discovered X-ray mode switching supports a local or global magnetospheric interpretation.

To build on the PSR B0943+10 discoveries, we therefore searched radio and X-ray catalogues for an attractive alternative radio pulsar known to exhibit mode switching with mode occurrence fractions between ~ 30 per cent and 70 per cent (to enable statistically valid X-ray photon counts in both modes) and also reported to be an X-ray source. We did not find a suitable candidate there, but, searching the X-ray archives, we found that PSR B1822–09 had been in the *XMM–Newton* field of view in a short observation, in which we detected the X-ray counterpart. This pulsar has a younger characteristic age of 233 kyr and a shorter spin period $P = 0.769$ s (compared with 5 Myr and 1.1 s for PSR B0943+10). It has many properties in common with PSR B0943+10, but also peculiarly different characteristics. Like PSR B0943+10, PSR B1822–09 also switches between a bright ‘B’ mode and a quiet ‘Q’ mode in its radio main pulse (MP), but on shorter time-scales averaging a few minutes (compared with several hours for PSR B0943+10). Most remarkably, its Q mode exhibits an interpulse (IP), located at about half a rotation period from the MP, which switches mode in anti-correlation with the MP (Fowler, Morris & Wright 1981; Fowler & Wright 1982; Gil et al. 1994). The B mode, in contrast to PSR B0943+10, exhibits a brighter but more complex MP as well as a precursor component (PC) some 15° longitude prior to the MP, but a barely detectable IP.

Both PSR B0943+10 and PSR B1822–09 exhibit mode-dependent subpulse modulations, but of very different characters. PSR B0943+10’s B mode displays a very regular pattern of drifting subpulses with repetition period $P_3 \approx 2P$, while in its Q mode the emission is chaotic (Suleymanova & Izvekova 1984; Rankin & Suleymanova 2006). In the Q mode of PSR B1822–09 a strong modulation with long period $P_{3,Q} = (46.55 \pm 0.88)P$ has been found, but not showing organized drifting. In its B mode, a weak modulation is reported with a longer and apparently harmonically related periodicity of $P_{3,B} = (70 \pm 3)P$ (Latham, Mitra & Rankin 2012). Further recent and detailed descriptions of its modal and pulse-sequence behaviour are given by Backus, Mitra & Rankin (2010), Latham et al. (2012) and Suleymanova, Logvinenko & Smirnova (2012).

The natural interpretation of the 180° separation seen in the Q mode between the MP and IP is that PSR B1822–09 is an orthogonal rotator (see e.g. Hankins & Fowler 1986; Gil et al. 1994; Backus et al. 2010) with the MP and IP being produced above the magnetic poles, and both poles detected by our line of sight. This is an important difference to PSR B0943+10, which is believed to be rotating close to alignment ($\sim 9^\circ$) where our sight line continuously views one polar region. However, Dyks, Zhang & Gil (2005) and Malov & Nikitina (2011, 2013) pointed out that the MP–IP separation can also be explained in almost aligned rotator models. Given the importance of the geometry of PSR B1822–09 for the interpretation of the results of our X-ray/radio campaign and the absence of an exhaustive study of it in the literature, we have added such a study on the geometry of PSR B1822–09 in Appendix A. There, we concluded that the existing evidence strongly points to PSR B1822–09 as having an orthogonal rotator geometry.

We carried out an X-ray/radio campaign on PSR B1822–09 with *XMM–Newton* and simultaneous radio observations primarily with

Table 1. Jodrell Bank ephemeris of PSR B1822–09 valid during our *XMM–Newton* observations.

Right ascension (J2000)	$18^{\text{h}}25^{\text{m}}30^{\text{s}}.630(5)$
Declination (J2000)	$-9^\circ 35' 22'' 12(3)$
Epoch (TDB)	55836
ν (Hz)	1.300 368 146 29(1)
$\dot{\nu}$ (Hz s^{-1})	$-8.872 83(2) \times 10^{-14}$
$\ddot{\nu}$ (Hz s^{-2})	$-5.6(1) \times 10^{-25}$
Start (MJD)	54923
End (MJD)	56749
Solar system ephemeris	DE200

Numbers in parenthesis are the 1σ errors on the least significant digits.

the Westerbork Synthesis Radio Telescope (WSRT) at 1380 MHz, and supported by the Giant Metrewave Radio Telescope (GMRT) at 325 MHz and the Jodrell Bank Observatory Lovell telescope at 1420 MHz. We aimed at having two telescopes simultaneously observing the pulsar to both ensure that we can identify all mode switches, and also to simultaneously monitor the radio characteristics at different radio frequencies.

In Section 2, we present the radio observations and how we defined the radio-mode windows, and also report a surprising relationship found between structures in the distributions of mode durations in the B and Q modes and their underlying modulation periodicities P_3 . In the subsequent sections, we present the *XMM–Newton* X-ray observations (Section 3), the X-ray maximum-likelihood (ML) spatial analysis of the sky maps, revealing a hard-spectrum source at a distance of only 5.1 arcsec from PSR B1822–09 (Section 4), and the first detection of the X-ray pulsed signal from PSR B1822–09 folding in the timing analysis with an ephemeris derived from Lovell telescope radio monitoring of PSR B1822–09 (Section 5). In Section 6, we present the search for X-ray mode switching using a combined spatial and timing analysis. The spectral characterization of the total, pulsed and steady unpulsed X-ray emissions is performed in Section 7, followed by a summary of our findings in Section 8 and a discussion of them in Section 9. Finally, our overall conclusions are presented in Section 10.

2 RADIO OBSERVATIONS AND RESULTS

2.1 WSRT radio observations and analysis

We observed PSR B1822–09 with the WSRT using the tied-array mode, in which the individual signals of each dish are coherently summed to a single synthesized array beam by applying appropriate time and phase delays. Twelve of the 14^1 WSRT 25-m dishes participated in the observations, and the Pulsar Machine II backend (Karuppusamy, Stappers & van Straten 2008) was used to record baseband voltage data from 8×20 -MHz subbands together spanning frequencies of 1300–1460 MHz. We converted the baseband data to both folded (10-s subintegrations) and single-pulse archives using dSPSR^2 (van Straten & Bailes 2011) and an up-to-date ephemeris (see Table 1) provided by ongoing timing of PSR B1822–09 with the Lovell telescope (Hobbs et al. 2004). Using tools from the *PSRCHIVE 2* software suite (Hotan, van Straten & Manchester 2004; van Straten, Demorest & Osłowski 2012),

¹ The rest were unavailable because of maintenance and the transition of the telescope to a new receiver system.

² <http://dspr.sourceforge.net/manuals/dspr/>

Table 2. Radio observations of PSR B1822–09 in 2013 and 2014 with the WSRT, GMRT and Lovell telescope, together covering the simultaneous observations with *XMM–Newton* (Table 3).

Telescope	Date (yyyy-mm-dd)	Freq. (MHz)	Start (UT) (hh:mm)	End (UT) (hh:mm)	Duration (h)
WSRT					
	2013-09-10	1380	14:52	22:22	7.49
	2013-09-18	1380	13:01	15:04	2.06
	2013-09-18	1380	15:15	20:31	5.25
	2013-09-22	1380	12:56	20:45	7.82
	2013-09-28	1380	12:49	20:18	7.50
	2013-09-30	1380	13:17	21:36	8.33
	2013-10-06	1380	12:22	19:12	6.83
	2014-03-10	1380	06:22	10:22	4.00
	2014-03-10	1380	10:26	11:56	1.50
	2014-03-12	1380	06:34	10:34	4.00
	2014-03-12	1380	10:38	11:48	1.16
GMRT					
	2013-09-10	338	13:15	18:42	5.45
	2013-09-18	624	17:35	18:12	0.62
	2013-09-22	624	11:37	18:06	6.48
	2013-09-28	624	09:32	17:30	7.95
	2013-09-30	624	09:36	17:20	7.73
	2013-10-06	624	10:41	17:01	6.33
Lovell					
	2013-09-10	1420	14:55	23:45	8.83
	2013-09-18	1420	17:05	19:47	2.70
	2013-09-22	1420	13:31	20:57	7.43
	2013-10-06	1420	14:30	19:13	4.72
	2014-03-12	1420	09:56	12:05	2.15

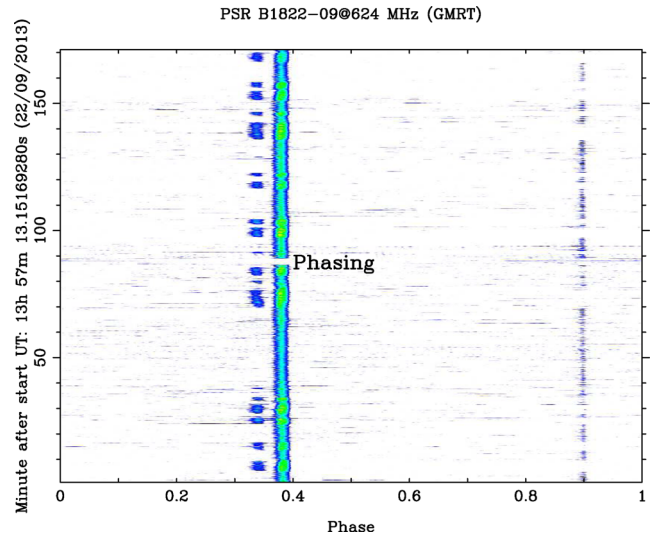
Table 3. *XMM–Newton* observations of PSR B1822–09 in 2013 and 2014.

Obs. ID	Date (yyyy-mm-dd)	Start time Pn/MOS [hh:mm (UT)]	End time Pn/MOS [hh:mm (UT)]
0720730901	2013-09-10	15:41 / 15:12	22:07 / 22:07
0720731001	2013-09-18	13:51 / 13:21	19:43 / 19:43
0720731101	2013-09-22	13:41 / 13:11	20:35 / 20:34
0720731201	2013-09-28	13:39 / 13:10	19:31 / 19:31
0720731301	2013-09-30	13:48 / 13:19	21:34 / 21:34
0720731601	2013-10-06	13:18 / 12:32	19:10 / 19:09
0720731401	2014-03-10	07:37 / 07:08	13:29 / 13:29
0720731501	2014-03-12	07:30 / 07:01	16:59 / 16:59

the data were cleaned of radio frequency interference (RFI) and the eight 20-MHz bands were combined into a single data cube of pulse phase, radio frequency and intensity (Stokes I). WSRT provided data during all (eight in total) *XMM–Newton* observing sessions, and covered practically all of the relevant X-ray windows (see Tables 2 and 3).

2.2 GMRT observations

Simultaneous PSR B1822–09 observations were carried out at the GMRT for the first six observing sessions in 2013 September and October, at 338 MHz on the first session and 624 MHz for the rest of the sessions (see Table 2). The GMRT is a multi-element aperture synthesis telescope (Swarup et al. 1991) consisting of 30 antennas distributed over a 25-km-diameter area that can be configured as a single dish in both coherent and incoherent array modes of operation. The observations discussed here used the coherent (or more commonly called phased array) mode (Gupta et al. 2000; Sirothia 2000). At these observing frequencies, the

**Figure 1.** GMRT observation at 624 MHz of PSR B1822–09, 2013 September 22, showing single-pulse sequences. Observation time versus pulsar phase: at phase ~ 0.34 the PC switches on/off; at phase ~ 0.38 the MP switches between the bright (B) and weaker quiet (Q) mode; at phase ~ 0.9 the IP switches on/off in anticorrelation with the MP and PC. There is some RFI as well, and that corresponds to the other features. Phasing: time in which there was no available data on PSR B1822–09 because the telescope needed to point to a calibration source.

GMRT is equipped with dual linear feeds that are converted to left- and right-handed circular polarizations via a hybrid. The dual polarization signals are passed through a superheterodyne system and down converted to the baseband that are finally fed to the GMRT software backend (Roy et al. 2010). In the backend, the FX correlator algorithm is implemented and in the phased array mode the voltage signals from all antennas are added in phase, which is finally recorded as a total power time series. We used a total bandwidth of about 33 MHz spread over 256 channels with time resolution of 0.122 ms.

The observing sessions at GMRT were such that only partial overlap, mostly during the earlier part of the observations, between WSRT, Lovell and *XMM–Newton* were possible. Even within the overlap region, some parts of the data were not usable due to RFI or technical problems. At GMRT frequencies, the strength of the IP is much more prominent than seen at higher frequencies, and hence the alternate emission between the IP and the PC for the Q and B modes, respectively, could be easily verified in these data. In regions of overlap with the WSRT observations, the mode switches were seen to correlate extremely well with what was derived based on the WSRT data. Fig. 1 shows as an example of the moding behaviour of PSR B1822–09 single-pulse sequences measured with the GMRT at 624 MHz covering part of one of our *XMM–Newton* observations. The MP and PC are shown to simultaneously switch on/off on short time-scales (typically minutes), while the IP switches on/off in anticorrelation with the MP and PC.

2.3 Lovell Telescope observations

We observed PSR B1822-09 using the 76 m Lovell Telescope at the Jodrell Bank Observatory on five occasions (Table 2) simultaneous with the *XMM–Newton* observations (Table 3). Observations were made using a dual-polarization cryogenic receiver at a central frequency of 1520 MHz with a total of about 380 MHz of useful bandwidth after removal of known and intermittent

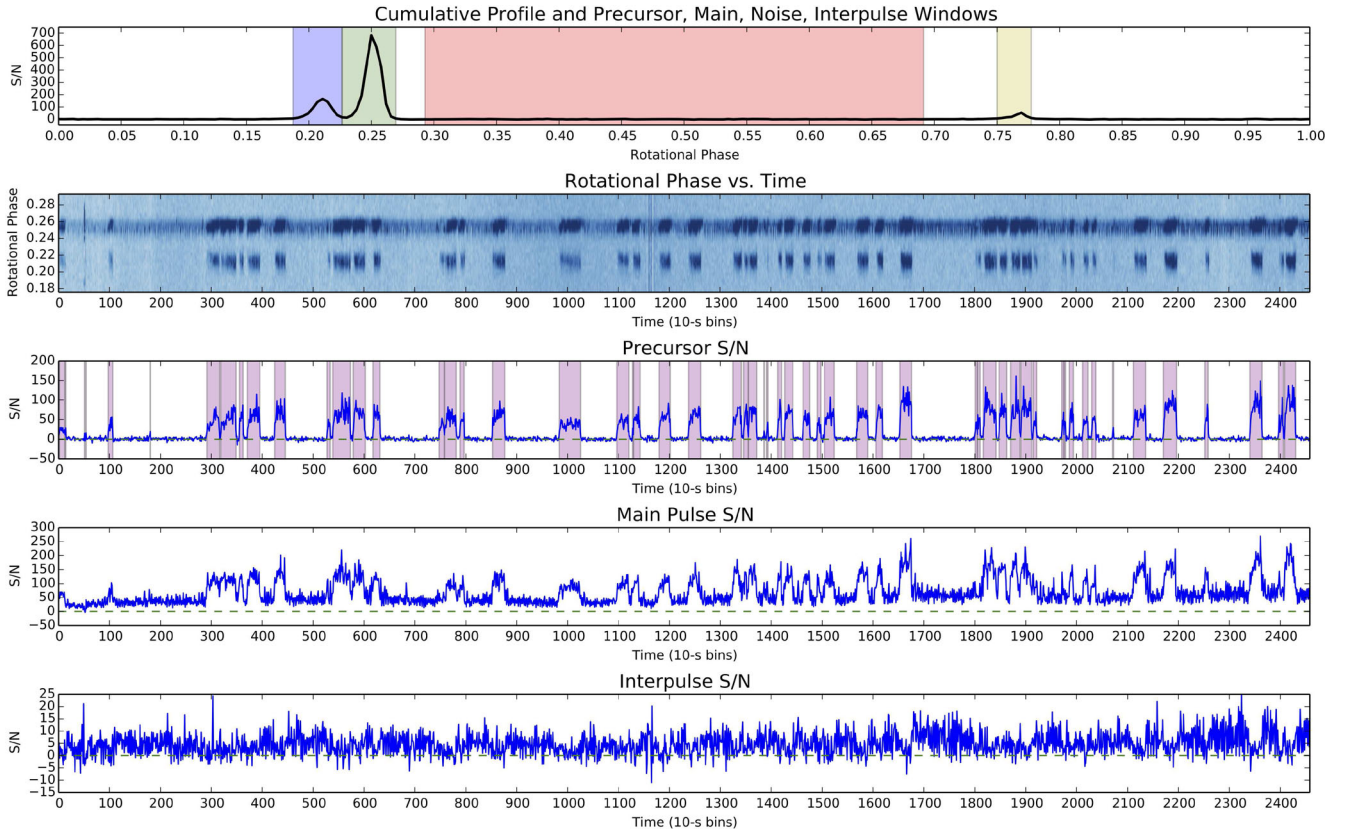


Figure 2. WSRT observation at 1380 MHz of PSR B1822–09 for 6.8 h, 2013 October 6. From top to bottom: cumulative pulse profile with indicated in colour the PC (purple), MP (green), off-pulse region / ‘Noise’ (orange) and IP (yellow) phase windows, followed by a zoom-in on the PC and MP as a function of time; then, the signal-to-noise ratios (S/N) of the detections in time bins of 10 s of the PC, the MP and the IP. The x-axis in the bottom four panels gives the number of 10-s bins. The PC exhibits a very clear on/off switching, and has been used to define the bright (B, pink) and quiet (Q) mode intervals.

radio-frequency interference. The incoming analogue data were sampled, dedispersed and folded in real-time using two different pulsar backends, the digital filter bank (DFB) and the coherent dedispersion backend called the ROACH³ (Bassa et al. 2016). The DFB data filtered the bandwidth into 0.5 MHz wide channels and incoherently dedispersed and folded into 10-s subintegrations using the same ephemeris as used for the WSRT observations. The ROACH data were coherently dedispersed and two data products were generated: folded profiles with 10-s subintegrations with 1 MHz wide channels and single-pulse archives with 4 MHz wide channels. The coherent dedispersion used the DSPSR (van Straten & Bailes 2011) software and post-processing made use of the PSRCHIVE software suite (Hotan et al. 2004; van Straten et al. 2012).

The Lovell telescope data overlapped with almost the entire WSRT data set and the *XMM–Newton* observing windows and so were used as an independent check of the detailed analysis of the WSRT data described below. A series of randomly chosen mode transitions were identified in the Lovell data, using either, or both, of the single-pulse and 10-s subintegration data and compared with those transitions identified in the WSRT data. These confirmed the times of the mode transitions and because of the different offsets between the start times of the 10-s subintegrations and single pulses could be used to estimate the maximum number of pulses that might be attributed to the incorrect mode.

2.4 Mode determinations using WSRT, Lovell and GMRT data

In our analysis, we make the basic assumption that, at any given time, PSR B1822–09 is either emitting in the B or Q mode. While this assumption seems to be strictly true for most mode-switching pulsars and was formerly thought to be true for PSR B1822–09, Latham et al. (2012) found evidence for short intervals of mixed modes in PSR B1822–09 in the vicinity of the transitions from one mode to the other with a duration of a few pulses. These intervals, however, are sufficiently short that they have little effect on our analysis.

Mode determination was based primarily on the WSRT data set because it provided the most complete overlap with the *XMM–Newton* sessions. The Lovell and GMRT data provided checks of the WSRT results, and the strategy of using three radio telescopes in parallel was to provide redundancy in the case of technical problems at one of the observatories during one of the *XMM–Newton* sessions (fortunately no such issues affected the general observing campaign).

Using WSRT data, we defined for each observation pulse-phase windows encompassing PSR B1822–09’s pulse PC, MP, IP and a reference off-pulse region (Fig. 2). For each 10-s subintegration (equivalent to ~ 13 pulse periods of $P = 0.769$ s) we measured the S/N of the PC, MP and IP (Fig. 2). We found that setting an S/N threshold on the precursor emission provided a robust and automated method of separating the B- and Q-mode intervals – despite the low number of pulses per 10-s subintegration. The presence of PC emission is in anticorrelation with the presence of the IP,

³ Reconfigurable Open Architecture Computing Hardware (ROACH) FPGA board developed by the Collaboration for Astronomy Signal Processing and Electronics Research (CASPER) group: <http://casper.berkeley.edu/>

but, the relative weakness of the IP at 1.4 GHz observing frequencies makes it a comparatively less reliable mode indicator. While PSR B1822–09 can sometimes switch modes on < 10 -s time-scales, such switches were not resolvable using this method. These intervals, however, are sufficiently short that they have negligible effect on the results of the X-ray analysis.

The first radio observations took place in 2013 September/October and comprised six sessions of between 7 and 8.5 h long (see Table 2), virtually contiguous with the times of the *XMM-Newton* observations listed in Table 3, amounting to a total of 162.620 ks (211 500 pulses). On the successive dates the Q-mode percentage was 65.1 per cent, 62.4 per cent, 60.6 per cent, 62.9 per cent, 66.6 per cent, 66.9 per cent, with an overall figure of 64.1 per cent. The second set of observations occurred on 2014 March 10 and 12 (Table 3). There were two sequences on each day, and the short second sequence of both had to be truncated (after 4 and 2.7 ks, respectively) as the pulsar was setting and the mode resolution poor. Altogether the useful observations amounted to 35.340 ks (46 000 pulses). The total Q-mode percentage of these observations was 63.5 per cent, giving a composite figure of 63.9 per cent for 2013 and 2014 together.

The total number of mode changes was 952, implying an average of one mode change every three and a half minutes (208 s). The average Q-mode sequence was 270 s (≈ 347 pulses), B-mode sequence 150 s (≈ 195 pulses). The longest Q mode was 4420 pulses (3400 s), recorded on September 28, and the longest B mode was 971 pulses (670 s) in the same observation and directly after the aforementioned long mode. Note that in a single 8-h observation (i.e. comparable with each of our observations) Latham et al. (2012) found examples of both Q- and B-mode lengths greater than those recorded here. An explanation for this possible discrepancy might be that some of our long mode windows are interrupted by a short (single 10-s integration) switch to the other mode that could in some cases be spurious and caused by RFI. For example, in Fig. 2 there is a very short ‘B-mode’ instance that breaks up what would be an otherwise longish Q-mode sequence. Alternatively, such short mode interruptions might have been overlooked by Latham et al. (2012).

It is relevant to note that Lyne et al. (2010) studied the spin-down of PSR B1822–09 in a sample of 17 pulsars over ~ 20 yr. The value of the $\dot{\nu}$ of PSR B1822–09 averaged over typically 50 d was found to change between two well-defined values, correlated with changes of the average pulse profile: for the high- $|\dot{\nu}|$ state, the precursor is weak and the IP is strong, with the reverse occurring for the smaller- $|\dot{\nu}|$ state. This correlation of large changes in $\dot{\nu}$ with pulse shape changes, found for a substantial number of pulsars, suggests a change in magnetospheric particle current flow. We verified that during all eight observing sessions of our campaign, the average $\dot{\nu}$ values of PSR B1822–09 were similar, not in a high- $|\dot{\nu}|$ state.

2.5 Mode-length histograms

Fig. 3 shows a histogram of the lengths of the intervals between the approximately 952 mode changes observed in 55 h, sampled every 10 s. If these were occurring at random it would imply a probability of $952/(55 \times 60 \times 6) = 0.048$ per 10 s. The associated exponential distribution describing the outcome of a Poisson process would be

$$N(x) = 952 \times 0.048 \exp(-0.048x). \quad (1)$$

Note that this curve closely matches the observations apart from the spike in the first single bin of 10 s (truncated in the figure), which contained 98 modes.

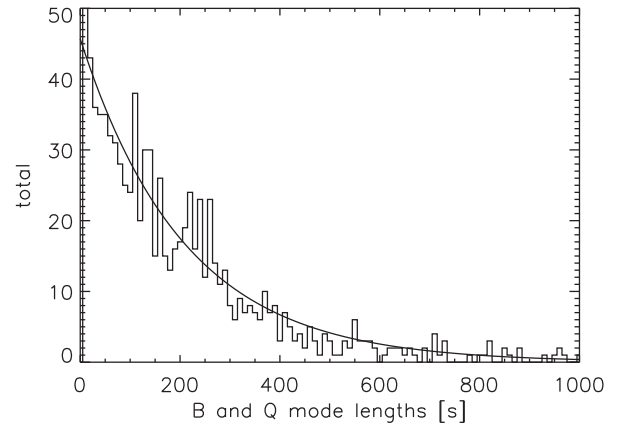


Figure 3. The histogram of the length of the intervals between the mode changes of PSR B1822–09. The data combine all observations in 2013 and 2014. The plotted exponential curve is the expectation if the mode changes occurred at random with a probability 0.048 per 10-s interval.

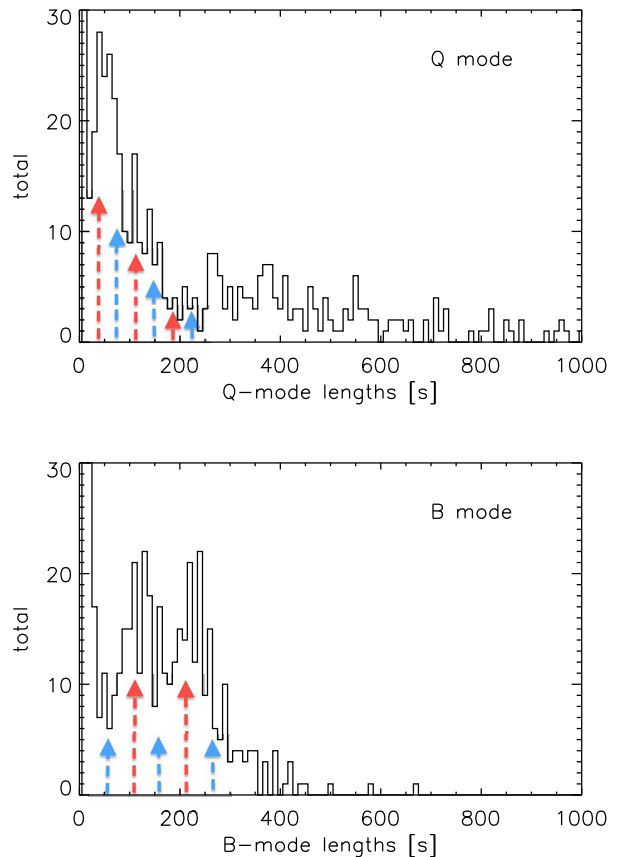


Figure 4. Upper figure: the histogram of the Q-mode lengths. Lower figure: the equivalent histogram for B mode. The red and blue lines show successive multiples of the P_3 for each mode reported by Latham et al. (2012). Note that red lines (odd multiples of P_3 for Q, even for B) tend to coincide with maxima, and blue lines (even multiples of P_3 for Q, odd for B) with minima. Since the P_3 s of Q and B (35.8 and 53.8 s, respectively) are resonant (2:3) the red lines at $3 \times 35.8 = 2 \times 53.8 = 107.4$ s and the red/blue lines at $2 \times 107.4 = 215.4$ s are common to both histograms.

Fig. 4 (upper) shows the histogram of the $\approx 952/2 = 476$ Q-mode lengths. In addition to the ultrashort modes of less than 20 s, we note a narrow peak at short lengths and a long trailing tail, suggesting the possibility of two kinds of Q-mode sequences (or three if we

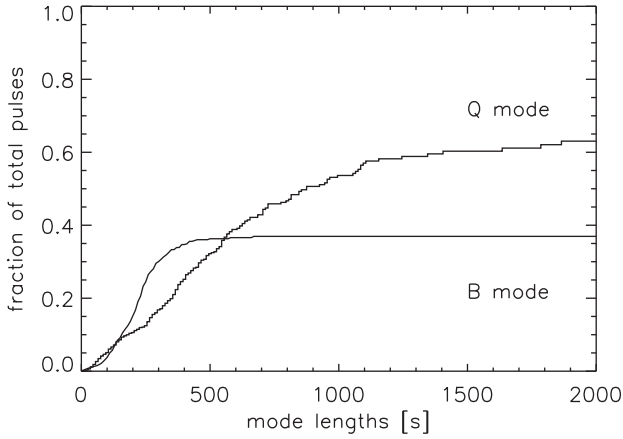


Figure 5. Cumulative distributions of the fraction of the total number of pulses, in separately the Q and B mode, as a function of mode length of PSR B1822-09.

include the ultrashort). Fig. 4 (lower) shows the histogram of the B-mode lengths. Apart from the spike in the first 10 s, it is noticeable that the distribution has two equal peaks (at ~ 120 and ~ 240 s) with a shallow dip between them. There is also a much shorter tail towards longer mode durations than in the Q-mode distribution.

Both the histograms of Fig. 4 have been overlaid with vertical red and blue lines that mark multiples of the central modulation periodicities (P_3) found by Latham et al. (2012) in 325 MHz observations of long Q- and B-mode sequences. Thus $P_{3,Q}$, expressed in terms of the rotation period P , is $46.55P$ (35.8 s) for the Q mode and $P_{3,B} = 70P$ (53.6 s) for the B mode, close to a ratio of 2:3. The markers appear to coincide with features in the histograms.

In Fig. 4 (upper) for the Q mode, the first (red) line closely aligns with the initial peak of the distribution, implying that the most common length for a Q-mode sequence, if one ignores the larger peak at the shortest time-scales, is the same as the modulation time-scale found in longer Q-mode sequences. It also suggests that all Q-mode sequences start at about the same phase of modulation.

We previously noted that both Figs 3 and 4 exhibit initial peaks for mode lengths ≤ 20 s and remarked earlier that mode switches on < 10 -s time-scales were not resolvable. In addition, RFI can mimic such short mode lengths and could be responsible for the initial peaks. In order to investigate how significant these short mode lengths might be for our analysis, we generated cumulative distributions of the fraction of the total number of pulses (\sim fraction of total observation time) in the Q and B mode as a function of mode length (see Fig. 5). This figure shows that the contribution of these short-length intervals amounts to < 1 per cent of the total number of pulses, thus can be ignored in the following discussion of the radio characteristics, as well as for the accumulation of X-ray events in the Q and B modes.

In the Q mode, at multiples of $P_{3,Q}$ little can be discerned as peaks or minima in the histogram, possibly because the decline in the height of the histogram is rapid and the bin size will smooth any features. However, a clear minimum appears around $6 \times P_{3,Q} = 215.2$ s. For this reason, we have given the $P_{3,Q}$ lines alternating colours of red and blue, speculating that there may be an unresolvable underlying periodicity of $2 \times P_{3,Q}$, corresponding to what is found in the B mode.

In the B-mode histogram of Fig. 4 (lower) a *minimum* appears at the $P_{3,B} = 70P = 53.8$ s (blue line), so B-mode sequences of this length are rare in the observations. Overwhelmingly, they are found near the first two multiples of $2 \times P_{3,B}$, i.e. 107.6 and 215.2 s (red

Table 4. Total lifetime (dead-time-corrected exposure) of our *XMM-Newton* observations of PSR B1822–09 for the MOS 1, MOS 2 and Pn cameras, and the corresponding lifetimes in the radio Q and B-mode time intervals. The radio observations covered about 87 per cent of the total *XMM-Newton* observations.

Camera	Total (ks)	Q mode (ks)	B mode (ks)
MOS 1	200,652	113,494	62,664
MOS 2	200,387	113,254	62,620
Pn	178,101	98,888	56,312

lines), separated by a further minimum at $\sim 3 \times P_{3,B} = 161.4$ s (blue line). This strongly supports the suggestion by Latham et al. (2012) that the precursor PC is modulated at $2 \times P_{3,B}$ and is weak where the MP is weak (Latham et al. 2012, see their fig. 12). As with the Q mode, the presence of peaks and troughs in the histogram implies that the B mode starts at roughly the same phase of its modulation.

Note that the cycle of maxima and minima in the two modes complement one another, with maxima in one roughly coinciding with minima in the other. In fact the B-mode maximum and Q-mode minimum at ~ 215.2 s ($=280P$) precisely coincide since $1/280$ is half the beat frequency of $1/46.55$ and $1/70$.

The important conclusion to be drawn from Fig. 4 is that for the first time in a mode-switching pulsar a clear yet subtle relationship has been found between the duration of its modes and a known underlying modulation time-scale of the intensities within the modes. It is all the more remarkable that in Fig. 3 the combined histogram of both modes suggests – possibly coincidentally – an overall random distribution of the mode lengths.

3 *XMM-Newton* X-RAY OBSERVATIONS

Before our work, only upper limits were published on X-ray emission from PSR B1822–09 (Alpar et al. 1995; Slane & Lloyd 1995). However, we found in the archives of *XMM-Newton* a short observation with an effective on-source exposure of 4.8 ks. We clearly detected the source at a significance level of 6.9σ (energies 0.2–2 keV) with a count rate slightly higher than what we had measured for the time-averaged count rate from PSR B0943+10, enabling us to propose this campaign. Later, Prinz & Becker (2015) also analysed this observation and found the source as well.

We obtained six *XMM-Newton* X-ray observations of PSR B1822–09 in 2013 September and October, and two in 2014 March with durations between ~ 6 and 9 h (see Table 3). In this work, we used only data obtained with the European Photon Imaging Camera aboard *XMM-Newton*, which consists of one camera based on Pn CCDs (Strüder et al. 2001), the Pn, and two cameras based on Metal Oxide Semi-conductor CCDs (Turner et al. 2001), MOS 1 and MOS 2. During all observations, the Pn camera was operated in large window mode, which provides a time resolution of 47.7 ms, and the MOS cameras were operated in small window mode with a time resolution of 0.3 s. For the three cameras, we used the thin optical filter. The EPIC Pn count rate in the 10–12 keV energy range was always significantly below 1.2 counts s^{-1} , indicating that our observations were not affected by increased particle backgrounds due to soft proton flares. The total lifetime (dead-time-corrected exposure) for the Pn, MOS 1 and MOS 2 cameras are given in Table 4.

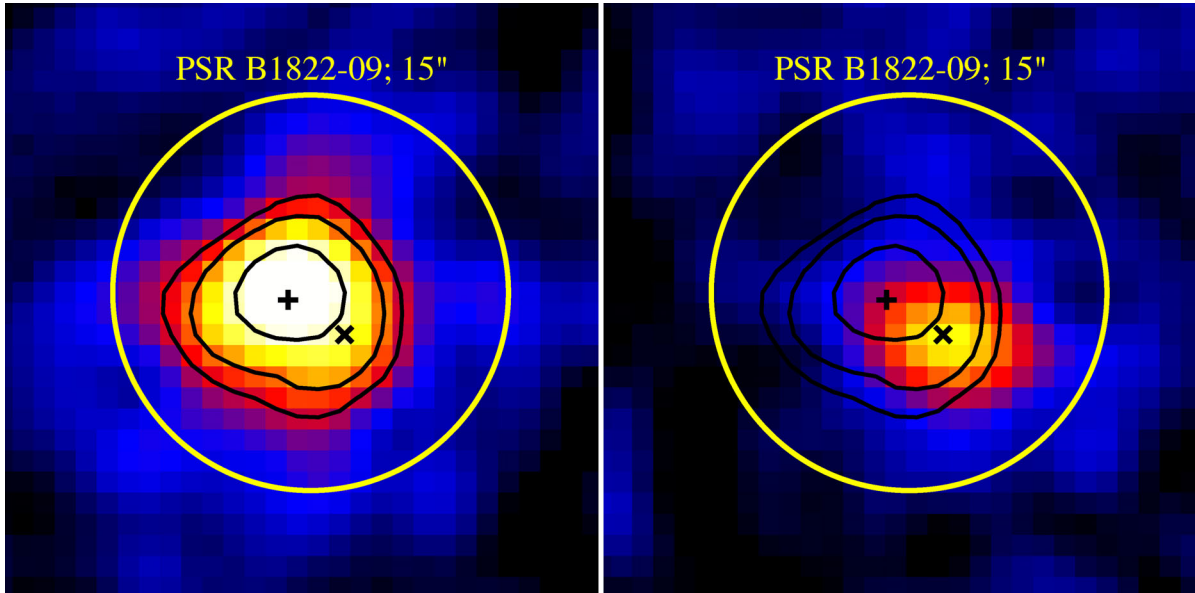


Figure 6. *XMM-Newton* MOS 1 and 2 images for energies 0.2–1.4 keV (left) and 1.4–10 keV (right), combining data from all eight observations. The yellow circles are centred on the radio position of PSR B1822–09 with radii 15 arcsec. The position uncertainty from radio timing is $\ll 1$ arcsec, see Table 1. The black contours represent contours of the image for energies 0.2–1.4 keV, shown in both images for comparison with the colour images. The X-ray position of PSR B1822–09 (+; with mean astrometric error of 1.25 ± 0.65 arcsec and negligible statistical uncertainty) and that of a nearby hard source at an angular separation of 5.1 ± 0.5 arcsec (x) are indicated. Below 1.4 keV the central excess is consistent with the presence of one source, positionally consistent with PSR B1822–09; above 1.4 keV also with only one source, the nearby hard source.

4 X-RAY SPATIAL ANALYSIS

In the spatial analysis, we apply a two-dimensional ML method using our knowledge of the two-dimensional point-source signature (the point spread function; PSF), and taking into account the Poissonian nature of the counting process. The PSF is fitted to the measured two-dimensional count distribution on top of a background structure, assumed to be flat, at the known position of the source or on a grid of positions in the source region when the source position is not known. Typical fit-region sizes are of the order of 30–60 arcsec.

At first the events⁴ are sorted in counts skymaps with two-dimensional pixels typically of size 2 arcsec \times 2 arcsec. To obtain the number of source counts the following quantity, $L = \ln \left(\prod_{i,j} (\mu_{ij}^{N_{ij}} \exp(-\mu_{ij}) / N_{ij}!) \right) = \sum_{i,j} N_{ij} \ln(\mu_{ij}) - \mu_{ij} - \ln(N_{ij}!)$, where $\mu_{ij} = \beta + \sigma \cdot \text{PSF}_{ij}$ is the expectation value for pixel (i, j) and N_{ij} the number of counts measured in pixel (i, j) , is maximized simultaneously with respect to the background parameter β and source scale parameter σ . The PSF is normalized to unity. Therefore, the total number of source counts σ (background free) is automatically obtained. The second derivative matrix of L evaluated at the optimum contains information about the uncertainties on the derived parameters, β and σ .

We applied this approach to the EPIC Pn and MOS 1 and 2 data (treating these separately), and obtained a very significant source excess at the position of PSR B1822–09. However, it turned out that this excess is not consistent with a single point source at the position of PSR B1822–09. This is already visible in the raw count maps, as

is illustrated in Fig. 6, which shows sky maps combining data from all eight observations with MOS 1 and 2 for energies 0.2–1.4 keV (left) and 1.4–10 keV (right). Below 1.4 keV the central excess is consistent with the presence of one source, positionally consistent with that of PSR B1822–09 and with a detection significance of 32.6σ (with 796 ± 38 counts assigned to the pulsar). From our X-ray analysis, we derived the following accurate position coordinates of PSR B1822–09: $\alpha_{2000} = 18^{\text{h}}25^{\text{m}}30^{\text{s}}.726$, $\delta_{2000} = -9^{\circ}35'23''.14$. The mean astrometric error for *XMM-Newton* is 1.25 ± 0.65 arcsec and the statistical uncertainties are negligible. The X-ray position is within 1.8 arcsec from the very long baseline interferometry radio position of Fomalont et al. (1992) and at ~ 1 arcsec from the Lovell timing position in Table 1. Also above 1.4 keV an excess is visible, but now shifted in position, with a detection significance of 14.4 sigma (with 268 ± 26 counts), and source position $\alpha_{2000} = 18^{\text{h}}25^{\text{m}}30^{\text{s}}.429$, $\delta_{2000} = -9^{\circ}35'25''.76$. The sources are thus separated by 5.1 ± 0.5 arcsec. The source positions are indicated in the figure. The independent EPIC Pn maps confirm these results.

4.1 Nature of nearby hard source?

The ML spatial analysis showed that the X-ray distribution can be explained with the presence of two point sources. However, given the 6 arcsec full width at half-maximum PSF of *XMM-Newton* and the measured separation of 5.1 ± 0.5 arcsec, we cannot exclude that the neighbouring excess is slightly extended. Of 13 nearby middle-aged pulsars with *XMM-Newton* and/or *Chandra* X-ray observations, six have prominent X-ray pulsar wind nebulae (PWNe), two have very faint PWNe and for four there are no detections reported yet in current data (Posselt, Spence & Pavlov 2015). For example, the most well-known nearby middle-aged pulsar Geminga exhibits a very prominent PWN, discovered by Caraveo et al. (2003) and more recently studied in most detail by Pavlov, Bhattacharyya

⁴ Each event i is characterized by its (barycentred) arrival time t_i , spatial coordinates x_i, y_i , energy E_i , event pattern ξ_i and flag F_i . We used $\xi_i = [0,4]$ and flag $F_i = 0$ for both Pn and MOS.

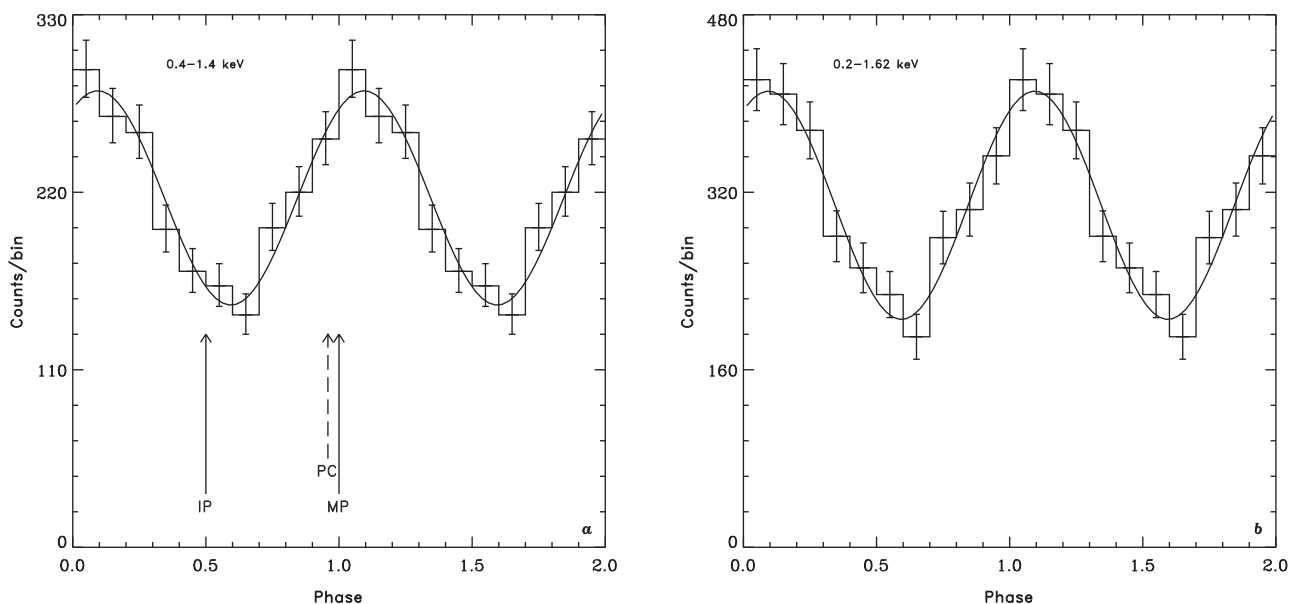


Figure 7. Pulse profile of PSR B1822–09, using data from *XMM–Newton* Pn and MOS 1 and 2 detectors for all eight observations. *Left*, (a), derived by phase folding of event arrival times (see text) for energies 0.4–1.4 keV selecting only events within an aperture of 20 arcsec; detection significance 9.6σ . *Right*, (b), derived by phase-resolved imaging (see text) for energies 0.2–1.62 keV, including all detected source events in the counts map; sky background has been modelled out. The radio MP peaks at phase 0. The solid-line profiles show fits with sinusoids peaking at phase 0.094 ± 0.017 . The arrows in (a) mark the phases of the radio MP, IP and PC.

& Zavlin (2010) exploiting deep *Chandra* observations. The latter authors confirmed that the Geminga PWN has three tail-like components with patchy structures, including three possibly moving blobs. The spectra of the PWN elements appeared to be rather hard with photon index ~ 1 . Our new source might be such a hard-spectrum element of a PWN of PSR B1822–09, but a deep high-spatial resolution *Chandra* observation is required to resolve the ambiguity of whether we are detecting in X-rays an extended structure or a compact object.

To investigate this further, we searched for a counterpart at lower energies by scrutinizing the optical/IR archives. We found deep (almost) on-source exposures performed on 2004 June 15 and July 20 by the ESO 3.6 m New Technology Telescope equipped with the 5.5 arcmin \times 5.5 arcmin CCD imaging camera SUSI2. We downloaded several images taken through different filters and correlated these with the UCAC3 catalogue for astrometric calibration yielding accurate positions at 0.1 arcsec level. In the 60, 600 and 800-s exposures (R , H_α and V bands, respectively), we found no candidate counterpart at the location of the hard source, nor at the position of PSR B1822–09, down to a limiting magnitude in the V band of ~ 25.0 , adopting an input spectrum of a A0 V star.

Independent of its nature, the discovery of this nearby hard source requires in our further analysis, notably when source spectra are derived, that both sources are fitted simultaneously for energies above 1.4 keV. For the *XMM–Newton* PSF and the low counting statistics of the new source, it suffices to assume a point-source structure.

5 X-RAY TIMING ANALYSIS

We performed timing analyses by selecting Pn and MOS 1 and 2 events detected within a 20 arcsec aperture around the X-ray position of PSR B1822–09. The times of arrival were converted to arrival times at the Solar system Barycentre and folded upon the ephemeris of PSR B1822–09 given in Table 1. Fig. 7(a) shows

the discovery of pulsed X-ray emission from PSR B1822–09 with the detection of a broad pulse in the energy band 0.4–1.4 keV at a significance of 9.6σ (Bucccheri et al. 1983, Z_1^2 value). The measured X-ray profile can be well fitted with a sinusoid and reaches its maximum at phase 0.094 ± 0.017 , with the radio MP, which is also sinusoidal in shape, peaking at phase 0 (indicated in Fig. 7a). The radio precursor precedes the radio MP, and the X-ray pulse lags the radio. Furthermore, we do not see a pulse or local maximum at the phase of the IP, something we might expect for the geometry of an orthogonal rotator. However, if there is a weaker X-ray pulse at the phase of the IP, also sinusoidal in shape, the summed profile with the MP would hide the X-ray IP and result in a phase distribution as shown in Fig. 7(a). Therefore we cannot state at this stage of the analysis, whether the measured distribution is due to two broad X-ray pulses, a strong one peaking close to the phase of the MP, and a weaker one peaking around the phase of the IP, or that we measure an unpulsed level of steady emission with a superposed single-pulse component. In the spectral analysis, we will address these two options.

The pulsar-phase distribution in Fig. 7(a) contains, in addition to pulsar-source counts (pulsed plus unpulsed), a flat celestial background level. This background level can be suppressed by applying phase-resolved spatial analysis: for each phase bin count sky maps are produced and with the two-dimensional ML method the number of source counts is determined per phase bin. This approach gives the distribution shown in Fig. 7(b) for the integral energy range 0.2–1.62 keV. All counts detected from PSR B1822–09 (pulsed plus unpulsed) are contained in this pulsar-phase distribution. Therefore, the number of source counts is much larger than in Fig. 7(a), because the latter contains only source counts (plus sky-background counts) detected within a 20-arcsec aperture around the PSR B1822–09 position, while the two-dimensional tail of the PSF extends well beyond the applied aperture. As a result, the energy range over which the pulse profile is detectable, widens somewhat.

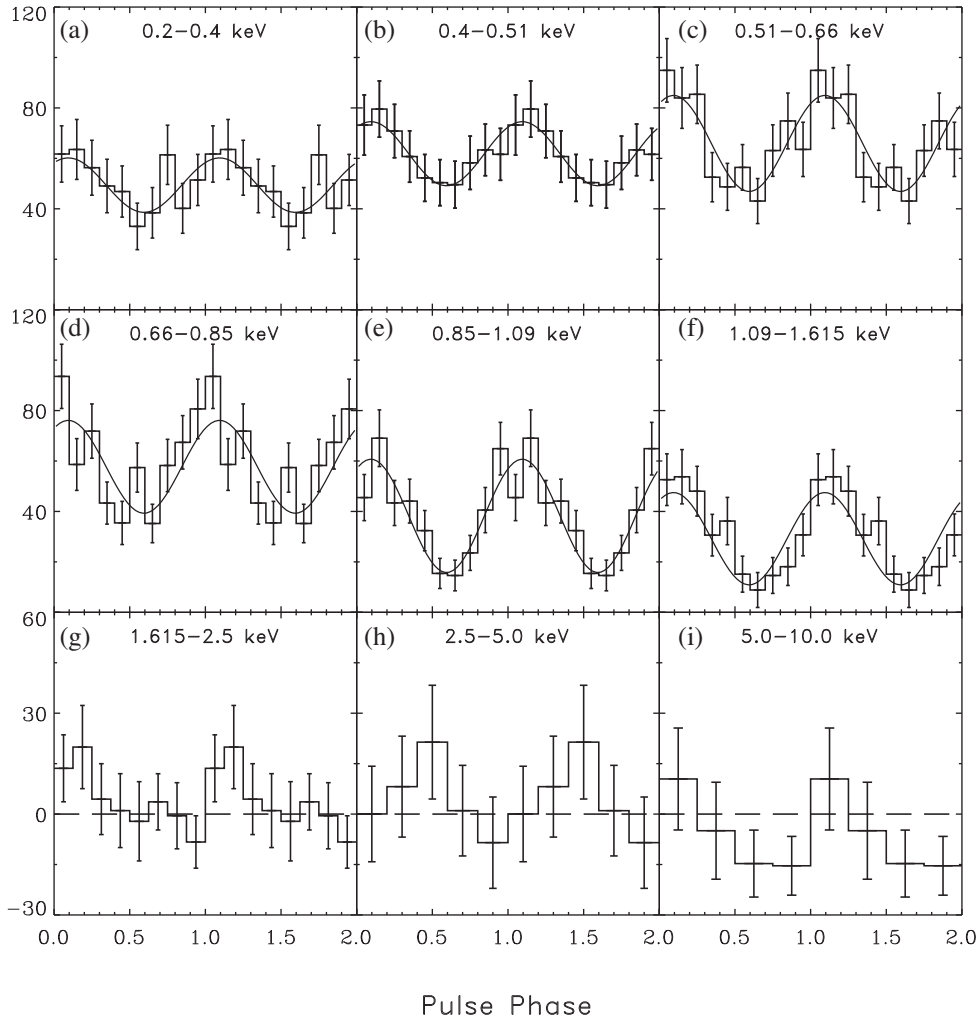


Figure 8. Pulse profiles of PSR B1822–09 in differential energy intervals between 0.2 and 10 keV, obtained from phase-resolved spatial analyses using *XMM–Newton* Pn and MOS 1 and 2 data for all observations listed in Table 3. The solid-line profiles show fits with a sinusoid centred on the phase of the X-ray pulse for the integral 0.4–1.4 keV energy interval. The radio MP peaks at phase 0. The celestial background, assumed to be flat, is modelled out. The y-axis gives per phase bin the derived number of pulsed plus unpulsed counts from the point source.

We applied the phase-resolved spatial analysis (all Pn and MOS 1 and 2, observations) in nine differential energy intervals between 0.2 and 10 keV. Fig. 8 shows the resulting pulse-phase distributions. From 0.2 to 1.6 keV, between ~ 300 and 700 source counts (pulsed plus unpulsed) are detected per energy interval, while above 1.6 keV the distributions are consistent with zero counts from PSR B1822–09 (the zero level is indicated by the broken line). This figure also shows that there is no evidence for a variation of the pulse shape with energy over the 0.2–1.6 keV band. Namely, for all phase distributions below 1.6 keV fits with sinusoids, with maximum at the same phase as shown in Fig. 7, above flat unpulsed source-count levels nicely represent the data, as is shown in the figure. Fig. 8 shows already by eye how the relative contributions of pulsed and unpulsed emission vary with energy.

In Fig. 8, it is apparent that the pulse profile is sinusoidal across the *XMM–Newton* energy band. We can therefore generalize the ML method by taking into account also the pulse-phase information of the events (three-dimensional approach), by assuming an energy-independent shape of the pulse profile. Sorting the events now according to their spatial (x , y) and pulse phase ϕ values, we can write for the expectation value of bin (i , j , k): $\mu_{ijk} = \beta + \sigma_u \cdot \text{PSF}_{ij} + \sigma_p \cdot \text{PSF}_{ij} \cdot \Phi_k$. In this formula, the value of the normalized

pulse profile at bin k is represented by Φ_k , while σ_u and σ_p correspond to the unpulsed and pulsed component scale factors. From σ_u and σ_p , the pulsed fraction η can be determined as $\eta = 1/(1 + (N_\phi \cdot \sigma_u/\sigma_p))$, with N_ϕ the number of bins of the normalized pulse profile.

Applying the three-dimensional ML method, we derived the pulsed fraction as a function of energy, shown in Fig. 9. At low energies of ~ 0.3 keV the pulsed fraction starts at a level of ~ 0.15 and reaches a value of ~ 0.6 around 1 keV. This clearly shows that the X-ray spectrum of the pulsed signal is much harder than that of the unpulsed emission. In Section 7.2, we will derive the corresponding spectral parameters.

6 X-RAY MODE SWITCHING

We have sorted the events collected in the radio Q- and B-mode time windows, respectively, as determined in Section 2.4 using our simultaneous radio observations. The accumulated lifetimes in the two radio modes of the MOS 1, MOS 2 and Pn cameras are listed in Table 4. For both modes, we applied the two-dimensional ML method in the 0.4–1.4 keV band on the pulsar position using the Pn and MOS 1 and 2 data and determined the total pulsar count rates. It turned out that there is no significant difference in the total

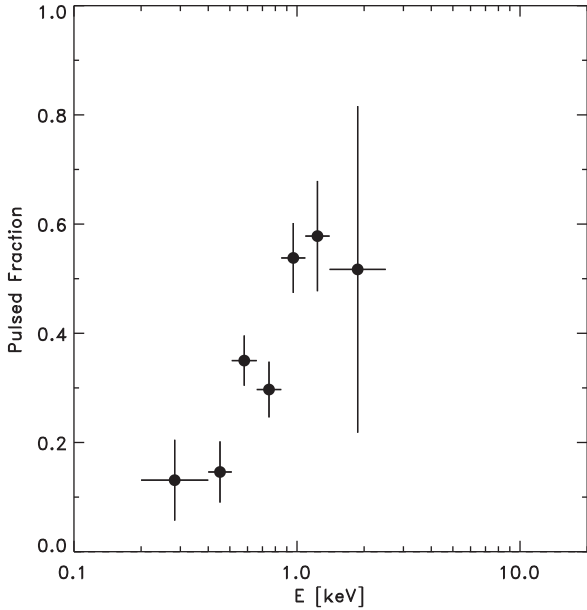


Figure 9. PSR B1822–09: pulsed fraction as a function of energy as derived from a three-dimensional ML analysis (see text). The energy dependence shown, indicates that between 0.2 and 2 keV the spectrum of the pulsed emission is harder than the spectrum of the unpulsed emission.

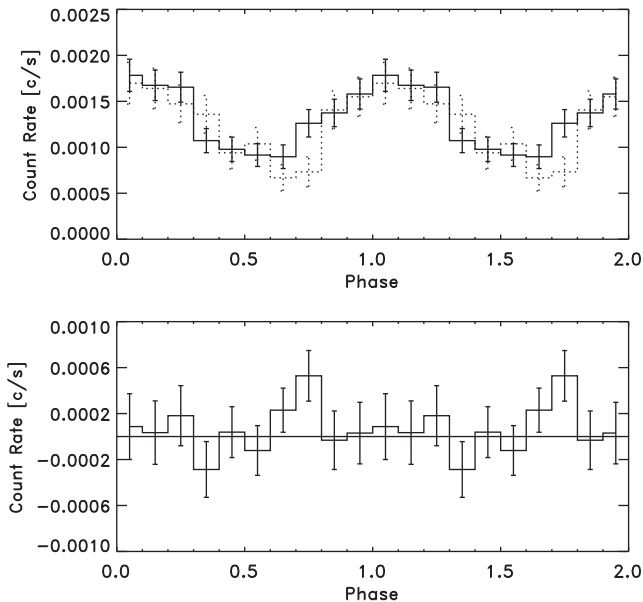


Figure 10. Pulse profiles of PSR B1822–09 obtained from phase-resolved spatial analyses using Pn and MOS 1 and 2 data. The celestial background is modelled out. Events are selected in the radio Q-mode (solid lines) or B-mode (broken lines) time windows for energies 0.4–1.4 keV. The pulse is detected in the Q and B mode. The probability that the two profiles are drawn from the same parent distribution is 97.5 per cent. The difference between the two mode-selected profiles is shown in the lower panel.

X-ray count rates of the Q and B modes, namely 0.0132 ± 0.0005 and 0.0126 ± 0.0006 , respectively. In order to check whether there is an indication for mode switching in the fluxes of the pulsed and unpulsed components, in the X-ray pulse shape, we constructed for the Q- and B-mode data pulse profiles of PSR B1822–09 applying phase-resolved spatial analysis, thus modelling out the celestial background. The pulse profiles (0.4–1.4 keV) are shown in Fig. 10

Table 5. PSR B1822–09 count rates ($\times 10^2$) in the energy band 0.4–1.4 keV for different selections on mode lengths in the Q and B modes.

Mode length	Total	10–210 s	≥ 210 s	
Q mode	1.32 ± 0.05	1.41 ± 0.13	1.29 ± 0.05	
Mode length	Total	0–50 s	50–160 s	≥ 160 s
B mode	1.26 ± 0.06	1.59 ± 0.35	1.20 ± 0.13	1.24 ± 0.07

for the Q mode (solid line) and B mode (broken line). Applying the Kolmogorov–Smirnov test gives a probability that the two profiles are drawn from the same parent distribution of 97.5 per cent. The differences between the two profiles are shown in the lower figure. This leads to the conclusion that we find no evidence for mode switching in the pulsed emission of PSR B1822–09 (pulse shape and flux), nor in the flux of the unpulsed emission.

In Fig. 4, we showed that the mode-length distributions of the Q and B modes are very different. They exhibit different structures that suggest a relation between mode durations and modulation time-scales of the radio intensities within the modes. Although we do not have an explanation for this intriguing relationship, and do not know whether a relation with the X-ray flux can be expected, we made selections on the apparent components in the mode-length distributions to see whether we find variations in X-ray flux/count rate. In the Q-mode-length distribution, the initial spike below 10-s duration does not contain a sufficient number of counts, therefore we selected events detected in the narrow peak at ~ 50 s between 10 s and the minimum at ~ 210 s ($\sim 6 \times P_3$), and events in the trailing tail above 210 s. In the B-mode distribution, we selected events in the initial spike until the minimum at ~ 50 s ($\sim 70P$), the next component between 50 and 160 s ($\sim 3 \times P_3$), and finally all events detected in mode intervals with lengths longer than 160 s. The derived X-ray count rates for energies 0.4–1.4 keV are given in Table 5 in comparison with the count rates for the total Q and B modes (no selection on mode length). For both modes, the count rates in the differential mode-length intervals are within 1σ of the count rates measured for the total Q and B-mode data, respectively. Therefore, we do not see evidence for a relationship between the X-ray count rate and an underlying modulation time-scale of the radio intensities within the modes.

7 SPECTRAL ANALYSIS

7.1 Spectrum total emission of PSR B1822–09

We first derived the spectral parameters for the total emission from PSR B1822–09 between 0.2 and 10 keV using all the observations listed in Table 3 the Pn and MOS 1 and 2 data and performing the two-dimensional ML analysis. We applied the optimization scheme introduced in Section 4 for the spatial analysis for a grid of user-defined energy windows between 0.2 and 10 keV, again adopting for the event pattern $\xi = [0, 4]$ and for the flag $F = 0$. For energies below 1.4 keV we fitted with one source at the position of PSR B1822–09 and for energies above 1.4 keV we included the second source as well. This resulted in background free source count numbers per energy interval (EPIC Pn and MOS 1 and 2 treated separately). These source counts were converted to source flux values in a forward folding spectral fitting procedure assuming a spectral model and using proper response (`arf` and `rmf` files) and lifetime (dead-time-corrected exposure) information.

An important parameter in this spectral analysis is the absorbing column density towards PSR B1822–09, N_{H} . An estimate of this

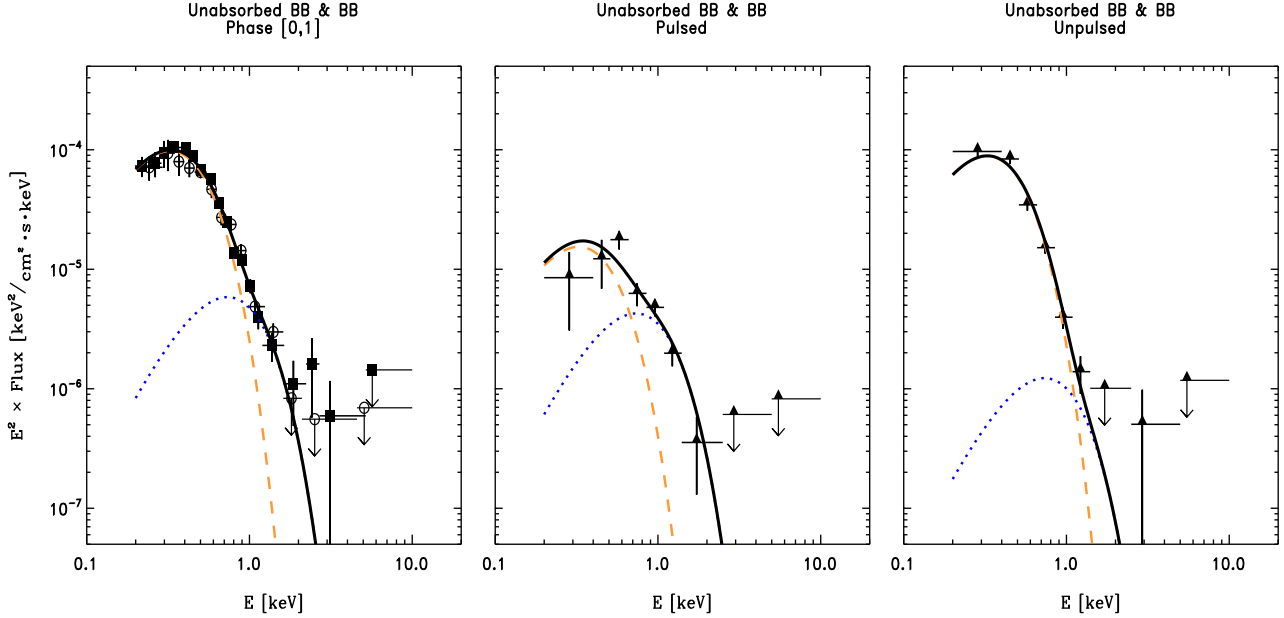


Figure 11. Unabsorbed X-ray photon spectra of PSR B1822–09. *Panel A:* Total spectrum from spatial analyses of count sky maps with flux values independently derived for *XMM–Newton* EPIC Pn (filled squares) and MOS 1 and 2 CCDs (open circles). The solid line shows the best fit with two blackbody (BB) components to the total spectrum (all phases); the broken orange line shows the contribution from the soft component ($kT = 0.83$ keV) and the dotted blue line the hot component ($kT = 1.87$ keV). *Panel B:* Fits with two BB components with the same kT values to the spectrum of only the pulsed emission, see text. *Panel C:* The same for the unpulsed/steady emission. In this case, the evidence for the hot component is marginal. Error bars are 1σ .

parameter is not yet published. Using H_I line measurements of pulsars, Johnston et al. (2001) determined an upper limit to the distance of PSR B1822–09 of 1.9 kpc, thus a location in front of the Sagittarius-Carina arm. We estimated that this would indicate an upper limit to N_{H} of $\sim 3 \times 10^{21} \text{ cm}^{-2}$. A number of papers quote a lower distance, e.g. 0.9 kpc (Zou et al. 2005; Prinz & Becker 2015). Therefore, we first treated N_{H} as free parameter in our spectral fits to verify whether its value from the X-ray spectral analysis will indeed be below the upper limit.

We first produced fits to the total source-count spectrum with a single PL (αE^{Γ}) and a single BB. Both fits are not acceptable. The PL index has an unphysical value $-6.32^{+0.30}_{-0.34}$ and the single BB gave a poor fit with $\chi_r^2 = 1.86$ (for 31 degrees of freedom, dof). A fit with a BB plus PL was also not acceptable with an unphysical value of Γ of $-5.1^{+0.60}_{-0.67}$. A fit with two blackbodies gave an excellent fit with $\chi_r^2 = 1.14$ (for 28 dof) and a very reasonable value for $N_{\text{H}} = 2.40^{+0.43}_{-0.42} \times 10^{21} \text{ cm}^{-2}$. In conclusion, the total spectrum of PSR B1822–09 can successfully be described as the sum of two BB components, a cooler BB with $kT \sim 0.083$ keV ($T \sim 0.96$ MK) and large hotspot radius of ~ 2 km, and a hotter BB with $kT \sim 0.187$ keV ($T \sim 2.2$ MK) and a radius of only ~ 100 m. Fig. 11(a) shows the excellent fit to the total spectrum with the two blackbodies. Table 6 lists all spectral parameters with their uncertainties of the discussed fits to the total emission. The best estimate of N_{H} from this X-ray analysis is for the two-BB fit ($2.40 \times 10^{21} \text{ cm}^{-2}$).

7.2 Spectra of the pulsed and unpulsed emissions of PSR B1822–09

In Section 5, we introduced the three-dimensional ML approach after we had shown that there is no evidence for pulse shape variations over the *XMM–Newton* energy range. In this approach, the ML analysis is applied in the 3D data space with axes the defined sky coordinates and the pulsar phase. The spatial PSF is the point-

Table 6. Spectral fits with power-law (PL) and BB models to the total emission spectrum of PSR B1822–09 over the energy range 0.2–10 keV using Pn and MOS 1 and 2 data of all observations listed in Table 3. The flux values are derived in a maximum-likelihood spatial analysis of sky maps for differential energy intervals.

Model	PL	BB	BB+PL	BB+BB
Fit par.	Total	Total	Total	Total
$N_{\text{H}} \times 10^{-21}$	$3.77^{+0.26}_{-0.23}$	$1.05^{+0.12}_{-0.12}$	$2.83^{+0.31}_{-0.25}$	$2.40^{+0.43}_{-0.41}$
$\alpha_{\text{PL}} \times 10^6$	$11.04^{+1.06}_{-1.04}$		$6.05^{+1.64}_{-1.70}$	
Γ	$-6.32^{+0.30}_{-0.34}$		$-5.10^{+0.60}_{-0.67}$	
$F_{\text{PL}} \times 10^{14}$	$8.19^{+0.20}_{-0.22}$		2.59 ± 0.20	
α_{BB_1}		$0.016^{+0.003}_{-0.002}$	$0.27^{+0.24}_{-0.12}$	$0.43^{+0.18}_{-0.14}$
kT_1		$0.126^{+0.003}_{-0.004}$	$0.085^{+0.007}_{-0.007}$	$0.083^{+0.004}_{-0.004}$
R_{BB_1}		393^{+37}_{-25}	1616^{+718}_{-359}	2039^{+389}_{-365}
$F_{\text{BB}_1} \times 10^{14}$		1.70 ± 0.04	2.27 ± 0.25	3.2 ± 0.2
$\alpha_{\text{BB}_2} \times 10^4$				10^{+12}_{-5}
kT_2				$0.187^{+0.026}_{-0.023}$
R_{BB_2}				98^{+48}_{-28}
$F_{\text{BB}_2} \times 10^{14}$				0.65 ± 0.11
χ_r^2 / dof	1.42 / 33-3	1.86 / 33-3	1.24 / 33-5	1.14 / 33-5

Units: N in cm^{-2} ; α_{BB} in $\text{ph cm}^{-2} \text{ s}^{-1} \text{ keV}^{-3}$.

kT in keV; fluxes are unabsorbed for the 0.5–2 keV band in $\text{erg cm}^{-2} \text{ s}^{-1}$; R_{BB} in metres adopting a source distance of 1 kpc; α_{PL} in $\text{ph cm}^{-2} \text{ s}^{-1} \text{ keV}^{-1}$ at 1 keV.

source signature in the sky maps for differential energy intervals and the sinusoid the shape of the pulse profile in all differential energy bins. The complementary pulsed and unpulsed source counts per differential energy interval are simultaneously determined. Similar to what has been done for the total spectrum, these source counts were converted to source flux values in a forward folding spectral

Table 7. Spectral parameters for single or double blackbody (BB) model fits to pulsed and unpulsed emission from PSR B1822–09 compared to the fit parameters for the double-BB fit to the phase integrated [0, 1] total emission (second column), the same as the last column in Table 6; third to fifth columns, for only the pulsed emission; sixth and seventh columns, for the unpulsed emission. The complementary pulsed and unpulsed emission spectra are simultaneously determined in a Maximum Likelihood analysis in the 3D data space with axes the sky coordinates and pulsar phase (see text). Bold values indicate the N_{H} and kT values fixed to the best-fitting values for the phase-integrated total emission. Fits are made over the energy range 0.2–10 keV using Pn and MOS 1 and 2 data of the observations listed in Table 3.

Model	BB+BB Total	BB Pulsed	BB+BB Pulsed	BB+BB Pulsed	BB Unpulsed	BB+BB Unpulsed
$N_{\text{H}} \times 10^{-21}$	$2.40^{+0.43}_{-0.41}$	2.40	2.40	2.40	2.40	2.40
$\alpha_{\text{BB}1}$	$0.43^{+0.18}_{-0.14}$		$0.034^{+0.164}_{-0.026}$	$0.068^{+0.015}_{-0.014}$	$0.39^{+0.13}_{-0.10}$	0.39 ± 0.02
kT_1	0.083 ± 0.004		$0.095^{+0.025}_{-0.021}$	0.083	0.083 ± 0.003	0.083
$R_{\text{BB}1}$	2039 ± 380		573^{+1382}_{-219}	811 ± 89	1940 ± 290	1940 ± 290
$F_{\text{BB}1} \times 10^{14}$	3.2 ± 0.2		0.75 ± 0.22	$0.46^{+0.10}_{-0.09}$	2.70 ± 0.14	$2.64^{+0.15}_{-0.13}$
$\alpha_{\text{BB}2} \times 10^4$	10^{+12}_{-5}	6.8^{+39}_{-25}	$7.2^{+19}_{-5.3}$	$7.3^{+0.9}_{-1.0}$		2.1 ± 1.0
kT_2	$0.187^{+0.026}_{-0.023}$	$0.136^{+0.010}_{-0.009}$	$0.181^{+0.050}_{-0.035}$	0.187		0.187
$R_{\text{BB}2}$	98^{+60}_{-25}	256^{+73}_{-47}	83^{+110}_{-31}	84 ± 5		45 ± 11
$F_{\text{BB}2} \times 10^{14}$	0.65 ± 0.11	1.12 ± 0.11	0.44 ± 0.15	$0.62^{+0.08}_{-0.08}$		0.18 ± 0.09
$\chi^2_{\text{r}} / \text{dof}$	1.14/33-5	1.37/9-2	1.44/9-4	1.42/9-2	2.06/9-2	1.81/9-2

Units: N in cm^{-2} ; kT in keV; α_{BB} in $\text{ph cm}^{-2} \text{s}^{-1} \text{keV}^{-3}$; R_{BB} in metre adopting a source distance of 1 kpc; fluxes are unabsorbed for the 0.5–2 keV band in $\text{erg cm}^{-2} \text{s}^{-1}$.

fitting procedure assuming a spectral model and using proper response (arf and rmf files) and lifetime (dead-time-corrected exposure) information.

In order to compare the fit parameters independent of variations in N_{H} , we fixed N_{H} in the following fits of the pulsed and unpulsed emission to the value obtained for the total emission with the double BB: $2.40 \times 10^{-21} \text{ cm}^{-2}$. First, we fitted the pulsed spectrum with a single PL, and could reject this shape (index $\Gamma = -4.3$ with $\chi^2_{\text{r}} = 1.87$ for 7 dof). However, a single BB rendered an acceptable fit ($\chi^2_{\text{r}} = 1.37$ for 7 dof) with $kT = 0.136^{+0.010}_{-0.009}$ keV and hotspot radius $R = 256^{+73}_{-47}$ m. The latter two values are in between those of the hot and cool components in the two-BB fit to the total emission (see second column of Table 7). When we then made a fit with a double-BB to the pulsed emission, we find within the statistical significance the same kT values for a hot and a cool component (fourth column) as for the total emission (second column). Although statistically not required, the double-BB fit thus renders a consistent picture with the same spectral components as obtained for the total emission. For further comparison, we also fixed the two kT values to the best-fitting values of the total emission (see the fifth column of Table 7). This interestingly shows that the flux of the hot component of the pulsed emission, with small radius of 84 ± 5 m, is consistent with being entirely responsible for the flux of the hot component in the total emission. The cool component of the pulsed emission contributes only a small fraction 14 ± 3 per cent to the flux of the cool component of the total emission. This indicates that the cool component ($kT = 0.083$ keV) should primarily be found in the unpulsed/steady component.

For the spectrum of the unpulsed emission, we could immediately rule out a PL shape ($\Gamma = -5.84$). A single-BB model gave a poor fit ($\chi^2_{\text{r}} = 2.06$ for 7 dof, or a 5 per cent probability for the fit to be acceptable), but with, interestingly, the same cool kT_1 value of 0.083 ± 0.003 keV and hotspot radius of ~ 2 km as found for the cool component in the total fit. To see whether there is also room for the above derived hot component, we added kT_2 fixed at 0.187 keV. The fit improved ($\chi^2_{\text{r}} = 1.81$ for 7 dof), but there is only marginal

evidence for this hot component; the flux has a 50 per cent error. The spectral fit parameters for the unpulsed-emission spectrum are also listed in Table 7.

Fig. 11(b) and (c) show the derived unabsorbed spectra of the pulsed and unpulsed emission, respectively. The best fits with two BB components (fixed at $kT = 0.083$ keV and $kT = 0.187$ keV) are shown, as well as the individual contributions of the cool and hot components. We obtained a consistent picture from this spectral analysis with the hot ($kT = 0.187$ keV) BB component in the total emission being due to the events in the pulse at the position of the MP above the flat/unpulsed level. There is not more than a hint for this hot component to be present in the unpulsed emission. Furthermore, the cool BB component with $kT = 0.083$ keV and radius of ~ 2000 m is almost entirely due to the unpulsed emission. In this case, such a cool component is also present in the pulsed emission but with smaller radius of ~ 800 m and contributes only a small fraction of ~ 14 per cent to the cool component in the total emission.

8 SUMMARY

Thanks to the long dead-time-corrected exposure of ~ 200 ks with *XMM-Newton*, together with the unprecedentedly long simultaneous WSRT radio coverage of PSR B1822–09 we could study its properties in great detail. We first present a summary of the new findings of our X-ray radio campaign.

(i) In ~ 198 ks of useful radio observations, 952 mode switches of PSR B1822–09 were detected with 63.9 per cent of the pulses in the Q mode. The average Q-mode length was 270 s (≈ 347 pulses), and average B-mode length 150 s (≈ 195 pulses).

(ii) The histograms of the radio Q-mode and B-mode lengths exhibit very different structures with maxima in one roughly coinciding with minima in the other, located at multiples of the modulation periodicity P_3 . For the first time in a mode-switching pulsar, this provides evidence for a relationship between the duration of its

modes and a known underlying modulation time-scale of the radio intensities within the modes.

(iii) In the X-ray spatial analysis, PSR B1822–09 was detected together with a nearby hard-spectrum X-ray source located at only 5.1 ± 0.5 arcsec from the X-ray position of PSR B1822–09 ($\alpha_{2000} = 18^{\text{h}}25^{\text{m}}30.726$, $\delta_{2000} = -9^{\circ}35'23''.14$). The new source dominates over PSR B1822–09 in skymaps for energies above 1.4 keV, and might be a PWN.

(iv) The observations revealed X-ray pulsations from PSR B1822–09 between 0.4 and 1.4 keV with a broad sinusoidal pulse detected at a significance of 9.6σ . The X-ray profile reaches its maximum at phase 0.094 ± 0.017 , slightly lagging the radio MP that peaks at phase 0, and is shifted in the opposite direction w.r.t. the position of the radio precursor at phase -0.042 (or 0.958).

(v) The X-ray phase distribution does not show an X-ray pulse at the phase of the radio IP, shifted by 180° w.r.t. the phase of the MP. If PSR B1822–09 emits an X-ray pulse at the phase of the IP, weaker than the X-ray pulse at the phase of the radio MP, but with similar sinusoidal shape, then we do not expect to see this pulse above an unpulsed level that is created by the sum of the X-ray IP and the same flux from the X-ray MP.

(vi) The pulsed fraction varies with energy from ~ 0.15 around 0.3 keV to a value of ~ 0.6 around 1 keV, indicative for a significant spectral difference between the pulsed and unpulsed emissions.

(vii) The observations did not reveal evidence for simultaneous mode switching in the X-ray and radio bands, nor in the X-ray pulsed emission (pulse shape or flux), nor in the flux of the unpulsed X-ray emission. The total count rate for energies 0.4–1.4 keV in the Q mode, $(1.32 \pm 0.05) \times 10^{-2}$, equals the count rate in the B mode, $(1.26 \pm 0.06) \times 10^{-2}$.

(viii) There is no evidence for a relationship between the X-ray count rate and the underlying modulation time-scale P_3 of the radio intensities within the modes. X-ray count rates for apparent different structures/components in the histograms of the radio Q-mode and B-mode lengths rendered the same count rates as obtained for the total Q and B mode.

(ix) The total X-ray spectrum is well described by a double BB model with a cool component with $kT = 0.083 \pm 0.004$ keV or $T = 0.96 \pm 0.05$ MK and a hot component with $kT = 0.187 \pm 0.026$ keV or $T = 2.17 \pm 0.30$ MK. The first has a hotspot radius of 2.0 ± 0.4 km and the latter 98_{-28}^{+48} m.

(x) The spectrum of the pulsed emission is well fit with a single BB, or a double BB with temperatures that are consistent with the values obtained for the hot and cool components in the spectrum of the total emission. For the latter fit, the flux of the hot component ($kT \sim 0.187$ keV with hotspot radius of ~ 84 m) is consistent with the flux of the same component in the total-emission spectrum.

(xi) The spectrum of the complementary unpulsed emission is almost entirely explained by the cool BB component with $kT = 0.083$ keV and hotspot radius of ~ 2000 m. This fit can be somewhat improved by adding a small contribution of the hot component identified in the total spectrum.

9 DISCUSSION

To date, long simultaneous X-ray and radio campaigns on mode-switching pulsars have only been performed on PSR B0943+10 and PSR B1822–09. For PSR B0943+10, Hermsen et al. (2013) discovered simultaneous mode switching in X-ray and radio emissions, not seen in our campaign on PSR B1822–09. What causes the simultaneous mode switching is still an enigma. For PSR B0943+10,

and now also for PSR B1822–09, the pulsed X-ray signals were detected for the first time, and the X-ray pulse profiles are similar; both exhibit a single sinusoidal pulse on top of unpulsed emission from the pulsars. This seems remarkable, because PSR B0943+10 is reported to be a nearly aligned rotator with our line of sight passing near the pole (Deshpande & Rankin 2001). Therefore, we continuously view isotropic thermal emission from one single pole of this pulsar, and no pulsation of thermal emission is expected. For PSR B1822–09, we conclude in Appendix A that the existing evidence of the known radio characteristics of PSR B1822–09 strongly suggests this pulsar as having an orthogonal rotator geometry with our line of sight close to the equator. In this case, we view such thermal emission from hotspots on both poles every rotation. Further in the discussion, we will address similarities of, and differences between these two pulsars where appropriate.

9.1 The nature of the radio modes

The contrast between the two radio modes of PSR B1822–09 could hardly be greater, going well beyond their original nomenclature of B ('bright') and Q ('quiet'): in Fig. 2 the precursor (the best mode indicator and used here to define the mode) can be seen to sharply switch on and off in tandem with the intensity of the MP and in anticorrelation with the IP strength. Given the clear switch in X-ray emission found between the similarly named modes of PSR B0943+10, one might expect the same effect in PSR B1822–09.

However, we report here that no radio versus X-ray correlation has been found (a 15 per cent change in X-ray count rate could have been detected at an $\approx 3\sigma$ level), and it is interesting to consider how PSR B1822–09 differs from PSR B0943+10. The most obvious difference is that the magnetic axis of PSR B1822–09 is almost certainly highly inclined to its rotational axis (see Appendix), while PSR B0943+10 is in near alignment. Another difference lies in the nature of the modal modulations found in both pulsars. In PSR B0943+10, the B mode exhibits a highly regular and rapid ($\sim 2P$) P_3 periodicity that may last for several hours, while in the Q mode this modulation vanishes and is replaced by highly disordered emission. The conventional interpretation of this is that a precisely circulating carousel on the polar cap dissolves and is replaced by chaotic discharging until the order is suddenly recovered. Thus, the mode lengths far exceed the subpulse modulation time-scale.

In contrast, PSR B1822–09 has been found to have modulation in both modes, both on a much longer time-scale ($\sim 46.6P$ and $70P$) than that of PSR B0943+10 and, significantly, not showing any subpulse 'drift' found in carousel-driven modulation (not for orthogonal rotators though). The modulated emission is diffuse against a steady background (and often hard to discern). This suggests a different physical mechanism and the fact that both the mode change and the modulations occur simultaneously at both poles suggests that both reflect magnetospheric effects, rather than local polar cap physics.

In light of this, it is perhaps not surprising that we find a link between mode lengths and modulation periods in PSR B1822–09. In Fig. 4 (upper) we see that the most likely Q-mode length is just the Q-mode modulation period ($46.55P$) and in Fig. 4 (lower) that the most likely B-mode lengths are double and quadruple multiples of the B-mode modulation ($70P$). The further fact that the modulation periods of the two modes are harmonically related and that the modes probably (though this is unproven) start at the same phase of their modulations (either peak or trough) suggests that the modes may both be manifestations of a common underlying magnetospheric 'clock', possibly set by the inclination of the pulsar, the size of its light cylinder and its magnetic field strength.

This view has the advantage of divorcing the radio emission from polar cap conditions and suggesting a commonality to both modes, so that the uncorrelated thermal X-ray emission may indeed relate to an unchanging polar cap temperature. It is interesting to note that the two radio-detected pulsars of the ‘Three Musketeers’⁵ (PSR B0656+14 and PSR B1055–52) exhibit non-drifting modulations with time-scales of $20P$. In the case of PSR B0656+14, Weltevrede et al. (2006, 2012) identify two distinct kinds of polar cap radio emission, of which only the ‘spiky’ emission is modulated. It would be of interest to investigate this in further single-pulse studies of PSR B1822–09. The modulated and unmodulated radio emission could be identified with the two distinct pulsed BB components already inferred for the X-ray emissions of PSR B0656+14, PSR B1055–52 and Geminga by De Luca et al. (2005) and proposed here for PSR B1822–09.

9.2 PSR B1822–09, a middle-aged pulsar like the Three Musketeers?

The total emission spectrum of PSR B1822–09 was well described by the sum of a hot BB and a cool BB spectrum. This differs from our findings for PSR B0943+10. In that case the total emission spectrum appeared to be the sum of a hot BB and a PL spectrum. PSR B0943+10 has a long spin period of 1.1 s and is relatively old (5 Myr) compared to PSR B1822–09 that has a shorter period of 0.77 s and is younger (233 kyr). Also, the spin-down luminosity of PSR B1822–09 is a factor ~ 40 (4.6×10^{33} erg s^{–1}) larger than that of PSR B0943+10. The characteristics of PSR B1822–09 might better be compared with those of the Three Musketeers. These pulsars have similar characteristic ages, but rotate a factor 2–4 faster with spin-down luminosities up to a factor ~ 8 larger than PSR B1822–09. The Three Musketeers exhibit in the 0.2–8 keV band spectra with three components: a cool BB ($T = 0.50$ – 0.79 MK), a hot BB ($T = 1.25$ – 1.90 MK) plus a PL component that contributes negligibly below ~ 2 keV and dominates above (see De Luca et al. (2005)). The two BB components of PSR B1822–09 have temperatures only slightly higher than those of the Three Musketeers and the fluxes of their PL components are too low for detection when scaled to the an-order-of-magnitude-lower count rate from PSR B1822–09.

The Three Musketeers have also been detected at high-energy gamma rays above 100 MeV, requiring a very hard steepening PL spectrum above the X-ray band in order to bridge several decades in luminosity to the high-energy gamma-ray band. Given the resemblance with PSR B1822–09 in the X-ray band, we selected all *Fermi*-LAT Pass 8-event data collected between 2008 August 4 and 2015 December 9 (MJD 54682.897–57365.907) with PSR B1822–09 in the field-of-view (region-of-interest: circular aperture of radius 5° centred on the pulsar), and extended the Jodrell Bank ephemeris to cover this time window. Using *Fermi* Science Tools⁶ `gtselect` and `gtbary`, respectively, we further selected only events with `Evclass = 128`, `evtype = 3` and Earth zenith angle $< 105^\circ$, and barycentered the event arrival times using the Solar system

⁵ Becker & Trümper (1997) dubbed PSR B0656+14, PSR B1055–52 and Geminga / PSR J0633+1746 the Three Musketeers. These three middle-aged pulsars have similar characteristics and were the only pulsars in the first list of 27 X-ray detected pulsars that exhibited thermal X-ray components (then probably also by the Vela pulsar), which could be attributed to thermal emission from the neutron star stellar surface; so called cooling neutron stars.

⁶ <http://fermi.gsfc.nasa.gov/ssc/data/analysis/software/>

ephemeris file DE200. We selected events with energies above 300 MeV, because we expect rather hard gamma-ray emission from middle-aged pulsars. Namely, Posselt et al. (2015) list the 11 nearby middle-aged pulsars detected by the LAT. They have PL spectra with average index of ~ -1.1 and average exponential cutoff of ~ 1.3 GeV. We phase folded the barycentered arrival times of events that were detected from within an energy-dependent aperture around PSR B1822–09 that contains ~ 68 per cent of the point-source counts $\{\theta_{68\text{ per cent}}(\text{degree}) = 0.8 \times [E(\text{MeV})/1000]^{-0.75}\}$ (Abdo et al. 2009). We verified that for the energy range where we might expect to detect events from PSR B1822–09 (up to a few GeV) this parametrization is consistent with the most recent one derived for Pass 8-event data.⁷ The obtained pulse profile is shown in the bottom panel of Fig. 12. There is an indication for the detection of a pulsed signal at a significance level of $\sim 2.7\sigma$ (Buccheri et al. 1983, Z_1^2 value), or a 0.66 per cent chance probability. Fig. 12 shows the gamma-ray profile in comparison with those in the radio band for the Q and B mode and the X-ray profile. It is interesting to note that the maximum of the broad gamma-ray profile at phase 0.92 ± 0.05 approximately coincides in phase with the PC in the radio B mode, and is shifted by 3.3σ with respect to the maximum of the X-ray pulse at phase 1.094 ± 0.017 . We note, that the *Fermi*-LAT Third Source Catalog (Acero et al. 2015) does not report a source within a distance of a degree of PSR B1822–09.

9.3 Modelling of the pulsed fraction

The apparently (nearly) orthogonal rotator geometry of PSR B1822–09 seems difficult to reconcile with the energy dependence of the pulsed fraction, reaching a maximum value of ~ 0.6 at 1 keV, for a single hot ($T = 2.17 \pm 0.30$ MK) pulse on top of cool ($T = 0.96 \pm 0.05$ MK) unpulsed emission. In fact, we derived from the spectral analysis that the hot pulsed component has a pulsed fraction that could be as high as 100 per cent.

For an orthogonal-rotator geometry it is remarkable that we did not see evidence for an X-ray pulse in the pulse profile from the phase of the IP. However, as we discussed, such a pulse can be hidden in the pulse profile in a flat unpulsed emission level when the X-ray MP and IP both are sinusoidal. The fit with two BBs to the spectrum of the unpulsed emission gives a hint for the presence of a weak hot component. If this hot component in the unpulsed emission is genuine, then in first approximation ~ 50 per cent can be assigned to the MP and ~ 50 per cent to the IP (assuming both have a sinusoidal shape). The best-fitting flux values then suggest an IP flux of ~ 12 per cent of that of the MP and a pulsed fraction of just the hot component of ~ 0.8 . These high pulsed fractions cannot be produced by isotropic BB emission in hotspots with the same temperatures and areas on both poles for the geometry assigned to PSR B1822–09. When we take the approximate relation $F_{\text{BB}} \propto T^4$ then the temperature of the antipodal spot (for the same area) should be ~ 59 per cent of that of the hotspot producing the main X-ray pulse to reach a pulsed fraction of ~ 0.8 . This would mean a temperature of ~ 0.110 keV.

For PSR B0943+10, we obtained similarly high pulsed fractions (Hermesen et al. 2013), namely, the pulsed fraction in the Q mode of a single hot thermal pulse on top of non-thermal unpulsed emission increased from ~ 0.2 at 0.2 keV up to ~ 0.6 at 1 keV. Considering

⁷ http://www.slac.stanford.edu/exp/glast/groups/canda/lat_Performance.htm; http://fermi.gsfc.nasa.gov/ssc/data/analysis/documentation/Cicerone/Cicerone_LAT_IRFs/IRF_PSF.html

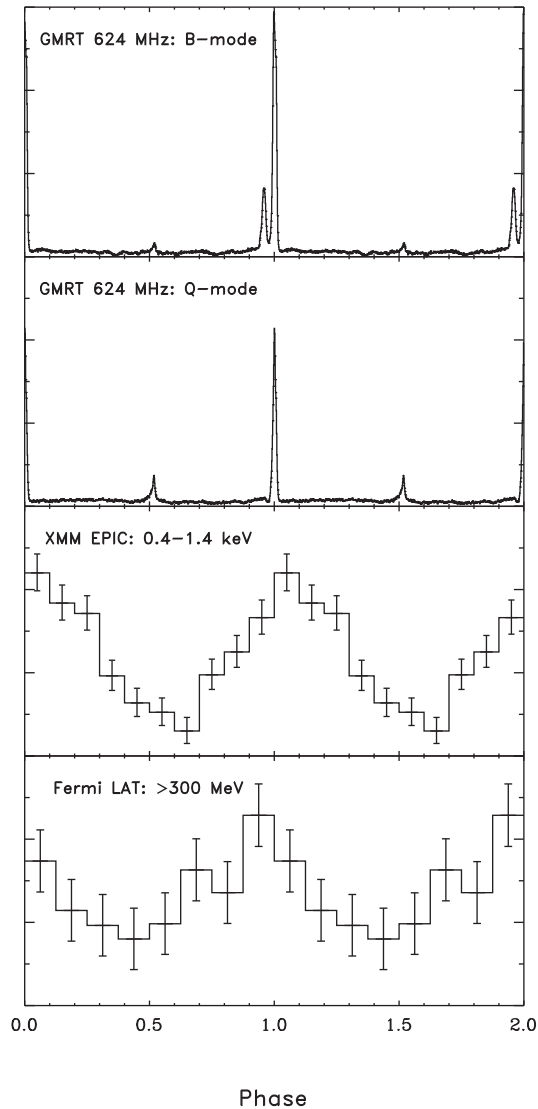


Figure 12. Pulse profiles of PSR B1822–09, from top to bottom: GMRT radio profiles at 624 MHz in arbitrary units for the B and Q mode, respectively; *XMM-Newton* EPIC X-ray profile for energies 0.4–1.4 keV; *Fermi* LAT profile for energies above 300 MeV. The vertical axes of the X-ray and gamma-ray pulse profiles are in counts/bin, and the error bars are statistical only (1σ).

just the thermal pulsed component in the Q mode, the modulation was also reported to be consistent with 100 per cent. These pulsed fractions are confirmed in the longer follow-up campaign on this pulsar (Mereghetti et al. 2016). PSR B0943+10 has an estimated magnetic field strength at the pole of 2×10^{12} G, significantly above a field strength of $B = 10^{11}(E/1 \text{ keV})$ G, when the electron cyclotron energy E_c exceeds the photon energy, and magnetic beaming makes the local emission essentially anisotropic (beamed along the direction of the magnetic field). The properties of a neutron star atmosphere (e.g. fully or partially ionized) determine the angular distribution and shape of the pulsations. The geometry and viewing angles determine finally what we observe. For example, Pavlov et al. (1994) showed that for a fully ionized neutron star atmosphere a strong narrow pencil beam along the magnetic field direction can be expected together with a broad fanlike component across the magnetic field. Even in the case of a uniformly heated neutron star surface the angular distribution is beamed along the magnetic

axis (Zavlin & Pavlov 2002). More recently, van Adelsberg & Lai (2006) also considered atmosphere models of magnetized neutron stars, and calculated characteristic beaming patterns exhibiting a thin pencil beam at low emission angles and a broad fan beam at large emission angles. See also similar work by Zane & Turolla (2006) and Turolla & Nobili (2013).

Stimulated by the discovery of simultaneous X-ray radio mode switching (Hermsen et al. 2013), Storch et al. (2014) considered a magnetized partially ionized hydrogen atmosphere model to explain the high pulsed fractions in the Q mode of PSR B0943+10, while remaining consistent with the nearly aligned dipole field geometry (Deshpande & Rankin 2001), and using the magnetic field strength of 2×10^{12} G inferred from its P and \dot{P} . They derived pulsed fractions ranging from 0.4 at 0.2 keV, up to a maximum of 0.9 at a few keV, which are higher than the pulsed fractions of the total emission. However, their calculations assumed just a single standard polar cap hotspot, and do compare well with, or are somewhat lower than, the measured values for the total emission when the calculated pulsed fractions are corrected (lowered) for the underlying unpulsed emission (see also Mereghetti et al. 2016).

PSR B1822–09 has an even stronger estimated magnetic field strength of 6.4×10^{12} G such that also for this pulsar magnetic beaming can shape the measured pulse profile. For its orthogonal geometry, we obviously need strong beaming effects such that hot X-ray emission from the IP is totally or mostly beamed away from our line of sight, while the X-ray emission from the MP passes through our line of sight. The cool unpulsed component in the total emission from PSR B1822–09, originating from an area with large radius of ~ 2 km, can be explained as the sum of broad pulses from both poles, possibly in fan beams. This would explain the finding that the estimated radius is significantly smaller than one expects for cool emission originating on the entire surface of the neutron star. This is in contrast to the cool areas found for e.g. the Three Musketeers, that are (more than) an order of magnitude larger, and their cool emission is thought to originate from the entire surface.

Following the above argumentation, if the thermal X-ray emissions from PSR B0943+10 and PSR B1822–09 are strongly beamed, and mode switching is due to some change in structure of the magnetic field, then for PSR B1822–09 the beaming angle of the X-ray pulsations might change less w.r.t. our line of sight between the B and Q mode than in a mode switch of PSR B0943+10. The lack of observable change in the pulse shape and brightness of PSR B1822–09 can then just be a coincidence of viewing geometry.

9.4 Conditions at the inner acceleration region

It is believed that the hotspots are actual polar caps heated by back-streaming ultrarelativistic particles accelerated in the inner acceleration region. Thus, the study of properties of hotspot components, such as size and temperature, can provide valuable information about this region of a neutron star. One can use the magnetic flux conservation law to estimate the magnetic field at the polar cap region $B_s = B_d R_{dp}^2 / R_{BB}^2$. Here, B_d is the dipolar component of the magnetic field at the polar cap, and R_{dp} is the radius given by the last open field line of the dipolar magnetic field component. Old pulsars with their spectrum dominated by hotspot radiation show that an actual polar cap is considerably smaller than R_{dp} , see e.g. PSR J0108–1431 (Pavlov et al. 2009; Posselt et al. 2012), PSR J0633+1746 (Kargaltsev et al. 2005), PSR B1929+10 (Misanovic, Pavlov & Garmire 2008). Furthermore, the estimated magnetic field strengths at the polar cap for these pulsars ($B_s \sim 10^{14}$ G) and temperatures of a few million Kelvin satisfy the condition for the formation

of a Partially Screened Gap (PSG) (see Gil, Melikidze & Geppert 2003; Medin & Lai 2007). Although, the fitted hotspot radius of PSR B1822–09 ($R_{\text{BB}} \sim 100$ m) is smaller than the conventional polar cap size ($R_{\text{dp}} = 165$ m) the derived magnetic field strength at the polar cap $B_s = 2.7 \times 10^{13}$ G and the fitted temperature $T \approx 2.2 \times 10^6$ K do not satisfy the condition for PSG formation (see equation 5 in Szary, Melikidze & Gil 2015). For such a high surface temperature and relatively weak surface magnetic field the outflow of thermal ions from the surface screens the gap completely. It is worth noting that both the size and temperature of the hotspot depend on the considered model. The atmospheric models, suggested by the high pulsed fraction, could result in different properties of the polar cap, and thereby different conditions in the inner acceleration region. But, an alternative acceleration mechanism might be at work, for instance the space-charged-limited flow model (Arons & Scharlemann 1979; Harding, Muslimov & Zhang 2002). In that case, surface charges can freely flow into the magnetosphere and the inner gap is thought to be space-charge limited. Pairs are created higher up in the magnetosphere near the so-called ‘pair-creation front’. Harding & Muslimov (2001) discuss pulsar polar cap heating and surface thermal X-ray emission in the case of Curvature Radiation pair fronts, and Harding & Muslimov (2002) in a second paper the case of Inverse Compton Radiation pair fronts. For the age and temperature of PSR B1822–09 only the first scenario might explain our measured thermal X-ray luminosity.

10 CONCLUSIONS

We have observed PSR B1822–09 for ≈ 55 h simultaneously at X-ray and radio frequencies. The X-ray results reveal a single-peaked, thermal sinusoidal pulse combining a small pulsed hotspot together with a 2 km-wide cooler region. Had we observed the pulsar at X-rays alone we might have concluded it was a middle-aged Geminga-like pulsar at low/intermediate inclination so that only a single polar hotspot is visible to us. This result was totally unexpected since it is known that at radio frequencies this pulsar displays an IP, and there is evidence from the polarization that its magnetic axis is highly inclined to the rotation axis – so why does not the X-ray emission have a double peak? We argued that a weak broad pulse could be hiding in the unpulsed emission.

A second puzzle arises from the lack of modulation in the X-ray pulse. For many years, it has been known that PSR B1822–09 switches in the radio band between two very distinctive modes of emission centred on the magnetic polar regions on a time-scale of several minutes. During our observations, we collected the largest ever number of mode transitions, and so for the first time we were able to build an overview of the statistics of the mode switches. These suggest a complex relationship between the durations of the modes and independently reported modulation time-scales present within each mode. Following the example of PSR B0943+10, where the pulsed and unpulsed X-ray emissions in its two radio modes differ in flux by a factor ~ 2 and the polar hotspot temperature seems to switch between two values (Mereghetti et al. 2016), one might expect a detectable modulated response also in the X-ray emission of PSR B1822–09. However, despite multiple attempts at matching our X-ray counts with aspects of the radio modulations, we found no correlation between the X-ray emission and simultaneously observed radio emission mode, e.g. the total count rates in the two modes are within ~ 5 per cent (1σ) the same. At face value, it seems that all the X-ray and radio emission of PSR B1822–09 have in common is the same rotation period and the same phase longitude for the MP.

Interpreting the X-ray observations of PSR B1822–09, we conclude that the X-ray emission may consist of emission from a principal small hotspot at the MP and two broader and cooler hotspots at the MP and IP phase, the first being ~ 35 per cent stronger than the latter. This may be explained by exploiting the effects of photon beaming in a strong magnetic field, with the hot X-ray IP not being directed towards us. In this context, it may be worth remembering that the radio MP/IP ratio is (also) quite extreme (see Fig. 12). Nevertheless, the puzzle remains as to why there appears to be no correlation between the thermal emission of the X-rays and the dramatic pan-magnetospheric mode changes implied by the radio emission. This outcome therefore forms an extreme contrast to the equivalent observations of the likely near-aligned pulsar PSR B0943+10 (Hermsen et al. 2013; Mereghetti et al. 2016).

One way out of this dilemma may be to argue that while the thermal X-rays come from the neutron star surface, the radio emission may originate from magnetospheric effects that do not directly impact the star’s polar caps or its wider surface. The polar interplay of the B and Q modes gives little doubt that some form of communication exists between the poles, and this must take place within the supposedly closed magnetosphere. Furthermore, it can be shown that the PSG (partly screened gap) mechanism for the production of polar cap patterns immediately above the surface will probably not work given the weak inferred magnetic field strength of PSR B1822–09. So an alternative mechanism, presumably operating at higher altitudes in the magnetosphere, must be responsible for the radio emission. Nevertheless, we still have to explain how the pulsar’s apparently unmodulated hotspot surface temperatures can be maintained at such high levels.

Finally, following the findings of Lyne et al. (2010) that PSR B1822–09 is one of a number of pulsars whose long-term profile modulations can be linked to changes in spin-down rates, it seems we must now come to the unexpected result that this pulsar’s thermal X-rays do not, or hardly, participate in the spin-down mechanism.

The results of our campaign on PSR B1822–09 have therefore raised more questions than answers. There is a clear disconnect between the radio and X-ray emission of this pulsar, and at times it has felt as though we are observing two different pulsars with the same period. One conclusion is certain: we are still far from understanding either the radio or the X-ray production mechanisms of pulsars.

ACKNOWLEDGEMENTS

We thank the staff of *XMM-Newton*, WSRT, GMRT and Lovell for making these observations possible. *XMM-Newton* is an ESA science mission with instruments and contributions directly funded by ESA member states and by NASA. The WSRT is operated by the Netherlands Institute for Radio Astronomy (ASTRON). GMRT is run by the National Centre for Radio Astrophysics of the Tata Institute of Fundamental Research. Pulsar research at the Jodrell Bank Centre for Astrophysics and the observations using the Lovell telescope is supported by a consolidated grant from the STFC in the UK. We thank Christine Jordan and Andrew Lyne for assistance with the data acquisition and Cees Bassa for developing the ROACH backend and for assistance with the data analysis.

ASTRON and SRON are supported financially by the Netherlands Organization for Scientific Research (NWO).

JMR acknowledges funding from US NSF grant 09-68296 and a NASA Space Grant. JWTH acknowledges funding from an NWO Vidi fellowship. JWTH and JvL acknowledge funding from the

European Research Council under the European Union's Seventh Framework Programme (FP/2007-2013) / ERC Starting Grant agreement nr. 337062 ('DRAGNET') and nr. 617199 ('ALERT'), respectively. AS acknowledges support by NWO under project 'CleanMachine' (614.001.301).

The *Fermi* LAT Collaboration acknowledges generous ongoing support from a number of agencies and institutes that have supported both the development and the operation of the LAT as well as scientific data analysis. These include the National Aeronautics and Space Administration and the Department of Energy in the United States, the Commissariat à l'Énergie Atomique and the Centre National de la Recherche Scientifique / Institut National de Physique Nucléaire et de Physique des Particules in France, the Agenzia Spaziale Italiana and the Istituto Nazionale di Fisica Nucleare in Italy, the Ministry of Education, Culture, Sports, Science and Technology (MEXT), High-Energy Accelerator Research Organization (KEK) and Japan Aerospace Exploration Agency (JAXA) in Japan, and the K.A. Wallenberg Foundation, the Swedish Research Council and the Swedish National Space Board in Sweden.

Additional support for *Fermi* science analysis during the operations phase is gratefully acknowledged from the Istituto Nazionale di Astrofisica in Italy and the Centre National d'Études Spatiales in France.

REFERENCES

- Abdo A. A. et al., 2009, *ApJ*, 699, L102
 Acero F. et al., 2015, *ApJS*, 218, 23
 Alpar M. A., Guseinov O. H., Kiziloglu U., Oegelman H., 1995, *A&A*, 297, 470
 Arons J., Scharlemann E. T., 1979, *ApJ*, 231, 854
 Backus I., Mitra D., Rankin J. M., 2010, *MNRAS*, 404, 30 (BMR10)
 Bassa C. G. et al., 2016, *MNRAS*, 456, 2196B
 Basu R., Mitra D., Rankin J., 2015, *ApJ*, 798, 105
 Becker W., Trümper J., 1997, *A&A*, 326, 682
 Blaskiewicz M., Cordes J. M., Wasserman I., 1991, *ApJ*, 370, 643 (BCW)
 Buccheri R. et al., 1983, *A&A*, 128, 245
 Camilo F., Ransom S. M., Chatterjee S., Johnston S., Demorest P., 2012, *ApJ*, 746, 63
 Caraveo P. A., Bignami G. F., de Luca A., Mereghetti S., Tur A., Becker W., 2003, *Science*, 301, 1345
 De Luca A., Caraveo P. A., Mereghetti S., Negroni M., Bignami G. F., 2005, *ApJ*, 623, 1051
 Deshpande A. A., Rankin J. M., 2001, *MNRAS*, 322, 438 (DR)
 Dyks J., Zhang B., Gil J., 2005, *ApJ*, 626, 45 (DZG05)
 Fomalont E. B., Goss W. M., Lyne A. G., Manchester R. N., Justtanont K., 1992, *MNRAS*, 258, 497
 Fowler L. A., Wright G. A. E., 1982, *A&A*, 109, 279
 Fowler L. A., Morris D., Wright G. A. E., 1981, *A&A*, 93, 54
 Gil J. A. et al., 1994, *A&A*, 282, 45
 Gil J. A., Melikidze G. I., Geppert U., 2003, *A&A*, 407, 315
 Gupta Y., Gothoskar P., Joshi B. C., Vivekanand M., Swain R., Sirothia S., Bhat N. D. R., 2000, in Kramer M., Wex N., Wielebinski R., eds, *ASP Conf. Ser. Vol. 202, IAU Colloq. 177: Pulsar Astronomy – 2000 and Beyond*. Astron. Soc. Pac., San Francisco, p. 277
 Hankins T., Fowler L. A., 1986, *ApJ*, 304, 256
 Harding A. K., Muslimov A., 2001, *ApJ*, 556, 987
 Harding A. K., Muslimov A., 2002, *ApJ*, 568, 862
 Harding A. K., Muslimov A., Zhang B., 2002, *ApJ*, 576, 366
 Hermsen W. et al., 2013, *Science*, 339, 436
 Hobbs G., Lyne A. G., Kramer M., Martin C. E., Jordan C., 2004, *MNRAS*, 353, 1311
 Hotan A. W., van Straten W., Manchester R. N., 2004, *PASA*, 302, 21
 Johnston S., Koribalski B., Weisberg J. M., Wilson W., 2001, *MNRAS*, 322, 715
 Kargaltsev O. Y., Pavlov G. G., Zavlin V. E., Romani R. W., 2005, *ApJ*, 625, 307
 Karuppusamy R., Stappers B., van Straten W., 2008, *PASP*, 120, 191
 Kramer M., Lyne A. G., O'Brien J. T., Jordan C. A., Lorimer D. R., 2006, *Science*, 312, 549
 Latham C., Mitra D., Rankin J., 2012, *MNRAS*, 427, 180
 Lorimer D. R., Lyne A. G., McLaughlin M. A., Kramer M., Pavlov G. G., Chang C., 2012, *ApJ*, 758, 141
 Lyne A., Manchester R. N., 1988, *MNRAS*, 234, 477
 Lyne A. G., Hobbs G., Kramer M., Stairs I., Stappers B., 2010, *Science*, 329, 408
 Malov I. F., Nikitina E. B., 2011, *Astron. Rep.*, 55, 1, 19
 Malov I. F., Nikitina E. B., 2013, *Astron. Rep.*, 57, 11, 833
 Medin Z., Lai D., 2007, *MNRAS*, 382, 1833
 Mereghetti S. et al., 2016, *ApJ*, 831, 21
 Misanovic Z., Pavlov G. G., Garmire G. P., 2008, *ApJ*, 685, 1129
 Mitra D., Rankin J. M., 2002, *ApJ*, 577, 322
 Pavlov G. G., Shibano Yu. A., Ventura J., Zavlin V. E., 1994, *A&A*, 289, 837
 Pavlov G. G., Kargaltsev O., Wong J. A., Garmire G. P., 2009, *ApJ*, 691, 458
 Pavlov G. G., Bhattacharyya S., Zavlin V. E., 2010, *ApJ*, 715, 66
 Pilia M. et al., 2016, *A&A*, 586, 92
 Posselt B., Arumugasamy P., Pavlov G. G., Manchester R. N., Shannon R. M., Kargaltsev O., 2012, *ApJ*, 761, 117
 Posselt B., Spence G., Pavlov G. G., 2015, *ApJ*, 811, 96
 Prinz T., Becker W., 2015, preprint ([arXiv:1511.07713](https://arxiv.org/abs/1511.07713))
 Radhakrishnan V., Cooke D. J., 1969, *ApJ, Lett.*, 3, 225
 Rankin J. M., 1990, *ApJ*, 352, 247
 Rankin J. M., 1993a, *ApJ*, 405, 285
 Rankin J. M., 1993b, *ApJS*, 85, 145
 Rankin J. M., Suleymanova S. A., 2006, *A&A*, 453, 679
 Roy J., Gupta Y., Pen U.-L., Peterson J. B., Kudale S., Kodilkar J., 2010, *Exp. Astron.*, 28, 25
 Sirothia S., 2000, M.Sc. thesis, Univ. Pune
 Slane P., Lloyd N., 1995, *ApJ*, 452, 115
 Storch N., Ho W. C. G., Lai D., Bogdanov S., Heinke C. O., 2014, *ApJ*, 789, L27
 Strüder L. et al., 2001, *A&A*, 365, L18
 Suleymanova V. A., Izvekova V. A., 1984, *Sov. Astron.*, 28, 32
 Suleymanova S. A., Logvinenko S. V., Smirnova T. V., 2012, *Astron. Rep.*, 56, 207
 Swarup G., Ananthakrishnan S., Kapahi V. K., Rao A. P., Subrahmanya C. R., Kulkarni V. K., 1991, *Curr. Sci.*, 60, 95
 Szary A., Melikidze G. I., Gil J., 2015, *MNRAS*, 447, 2295
 Turner M. J. L. et al., 2001, *A&A*, 365, L27
 Turolla R., Nobili L., 2013, *ApJ*, 768, 147
 van Adelsberg M., Lai D., 2006, *MNRAS*, 373, 1495
 van Straten W., Bailes M., 2011, *PASA*, 28, 1
 van Straten W., Demorest P., Osłowski S., 2012, *Astron. Res. Techn.* 9, 237
 Weltevredre P., Wright G. A. E., Stappers B. W., Rankin J. M., 2006, *A&A*, 458, 269
 Weltevredre P., Wright G. A. E., Stappers B. W., 2007, *A&A*, 467, 1163
 Weltevredre P., Wright G., Johnston S., 2012, *MNRAS*, 424, 843
 Zane S., Turolla R., 2006, *MNRAS*, 366, 727
 Zavlin V. E., Pavlov G. G., 2002, in Becker W., Lesch H., Trümper J., eds, *Proc. 270 Heraeus Seminar on Neutron Stars, Pulsars and Supernova Remnants*, MPE Rep. 278. MPE, Garching, p. 263
 Zou W. Z., Hobbs G., Wang N., Manchester R. N., Wu X. J., Wang H. X., 2005, *MNRAS*, 362, 1189

APPENDIX A: THE GEOMETRY OF PSR B1822–09

PSR B1822–09 exhibits two distinct emission modes. In its 'B'right mode it shows a MP along with a PC, and in its 'Q'uiet mode one sees a weaker and more complex MP along with an IP. This

IP is separated by almost exactly 180° (see Backus et al. 2010, hereafter BMR10), although strangely the MP and IP show correlated intensity fluctuations while in principal they should have independent emission characteristics (Fowler et al. 1981; Fowler & Wright 1982; Gil et al. 1994; Dyks et al. 2005). It is however this 180° separation seen in the Q mode between the MP and IP that leads one to conjecture that the pulsar might be an orthogonal rotator (e.g. Hankins & Fowler 1986; Dyks et al. 2005, hereafter DZG05; BMR10). Although two further checks are necessary to strengthen the orthogonal rotator argument: the first is that the 180° separation between the MP and IP is seen over the entire band of observable frequencies, and the second is that the linear polarization position angle (PPA) traverse should be adequately described by the rotating vector model (RVM). Unfortunately no exhaustive study of these effects exists in the literature, possibly due to the lack of high-quality single-pulse observations permitting separation and individual study of the B and Q modes.⁸ As pointed out by DZG05 the 180° MP–IP separation can also be explained in almost aligned rotator models where the MP and IP are produced by the line of sight cutting through two sides of the hollow conical emission beam. However in this case, due to radius to frequency mapping one expects to see the MP–IP separation evolving with frequency. The other alternative in the aligned rotator category is a single-pole model, wherein the line of sight always remains within the emission cone and under special situations emission components separated by 180° are seen. Although in these cases (often known as wide profile pulsars) a low level bridge of emission is expected between the profile components, which however is completely absent in PSR B1822–09.

A1 Fitting the RVM

We are in possession of the high-quality polarized single-pulse P -band GMRT observation that was used by BMR10. Here, we use this observation to explore whether the PPA traverse can successfully be fitted by the RVM. The top-left panel of Fig. A1 shows the single-pulse sequence of 2077 pulses while the top-right panel shows the PPA histogram (as a grey-scale in the bottom panel) for these pulses. Only those PPAs are shown in the histogram where the single-pulse linear polarization power exceeds five times the rms noise level. The red points with error bars show the average PPA traverse. It is clear from this plot that the single-pulse linear polarized power is strong for the MP and the PC, but weak for the IP. The bottom left and right plots show the PC and MP regions of the PPA histogram for the B and Q mode, respectively. Qualitatively, the PPA behaviour for these two modes is seen to be similar; it is the PPA distributions within the two modes that changes.

Fitting the RVM to these PPA traverses is definitely a challenge. The original version of the RVM introduced by Radhakrishnan & Cooke (1969) was advanced by Blaskiewicz, Cordes & Wasserman (1991, hereafter BCW) where the first-order special relativistic effects of aberration and retardation (A/R) were included. In the most general case, the RVM depends on five parameters namely α the angle between the rotation and dipolar magnetic axes, β the impact angle between the magnetic axis and the observer’s line of sight, the distance r_{em} from the centre of the neutron star, the fiducial phase

ϕ_0 , and the arbitrary shift of the PPA at the fiducial phase ψ_0 .

$$\psi = \psi_0 + \tan^{-1} \left(\frac{\sin(\alpha)\sin(\phi - \phi_0) - (6\pi/P)(r_{\text{em}}/c)\sin(\eta)}{\sin(\eta)\cos(\alpha) - \sin(\alpha)\cos(\eta)\cos(\phi - \phi_0)} \right). \quad (\text{A1})$$

Here, $\eta = \alpha + \beta$, ψ is the PPA, ϕ is the pulsar phase, P the pulsar period and c the velocity of light. The r_{em} term in the numerator is due to the A/R effects discussed by BCW, and for $r_{\text{em}} = 0$ the equation reduces to the usual RVM. For normal pulsars like PSR B1822–09, it is well known that the radio emission originates typically at an altitude of about 1–5 per cent of the light-cylinder radius, and the effect of A/R is to simply shift the PPA both in ψ and ϕ , keeping the functional form of the traverse similar. For the RVM fitting exercise below, we will hence keep $r_{\text{em}} \sim 500$ km such that the quantity $(6\pi/P)(r_{\text{em}}/c) \sim 0.04$, where $P = 0.769$ sec. The usual strategy for fitting equation (A1) is to guess values for ϕ_0 and ψ_0 , based on the PPA traverse, and search for the parameters α and β . Unfortunately, for a given set of α and β the RVM can only be distinguished at the wings of the MP provided the width of the MP exceeds typically beyond 30° . Certainly this is not the case for PSR B1822–09, where the MP is only about 12° wide. This essentially means that fitting the RVM will not yield meaningful constraints on α and β .

Let us illustrate the above point by doing the fits. We first choose the Q-mode profile where the effect of the PC is low and the MP is prominent. At this stage, we should ask why the PC is not included in the RVM fits, and the reason is that the PC observed in several pulsars appears to be a different emission component with no clear polarizational relationship to that of the MP. The shape of pulse profiles can usually be explained by the core-cone model where a central core emission component is surrounded by pairs of nested conal features. Cones are of two types, outer and inner. Outer cones show radius-to-frequency mapping (RFM), whereas the inner cones evolve with frequency much less than do outer cones. In a detailed study of pulsars with PC components by Basu, Mitra & Rankin (2015), the authors demonstrated that the location of the PC components w.r.t. the MP remain constant with frequency, whereas the components in the MP usually show the expected radius to frequency mapping. For PSR B1822–09 the PC–MP separation (estimated as the peak of the PC and that of the MP) is about 14.3° over the band from 243 MHz to 10.3 GHz, whereas the width (estimated using half power point) of the MP evolves from 8.1° to 3.6° over this frequency range (see their fig. 1 and table 2). Constancy of width with frequency is also a known property of inner cones within the core-cone model (Mitra & Rankin 2002). (PSR B1822–09’s leading PC component might be modelled as an outer cone where the usual trailing component is not seen; however, its lack of evolution with frequency strongly mitigates against this explanation.) The MP on the other hand can be classified as a triple under the core-cone model showing the usual inner cone lack of RFM. We will also not include the IP for fitting the RVM. There are several reasons for doing so, but the most important one is that the sensitivity of our data does not allow us to interpret the PPA traverse by disentangling its Orthogonal Polarization Mode behaviour.

Returning to fitting the RVM to the MP emission, we need to provide initial values for ϕ_0 and ψ_0 . We assign ϕ_0 (and read off the corresponding ϕ_0 value) as the phase corresponding to the peak of the Q-mode profile, which is also the peak of the central core component of the triple profile classified by BMR10. The PPA traverse at this phase shows an orthogonal jump, which is also characteristic of core emission. With these values a grid search was

⁸Note that the recent PhD thesis of Phrudth Jaroenjittichai, <https://www.escholar.manchester.ac.uk/uk-ac-man-scw:199950>, University of Manchester, dedicates a chapter to the study of PSR B1822–09.

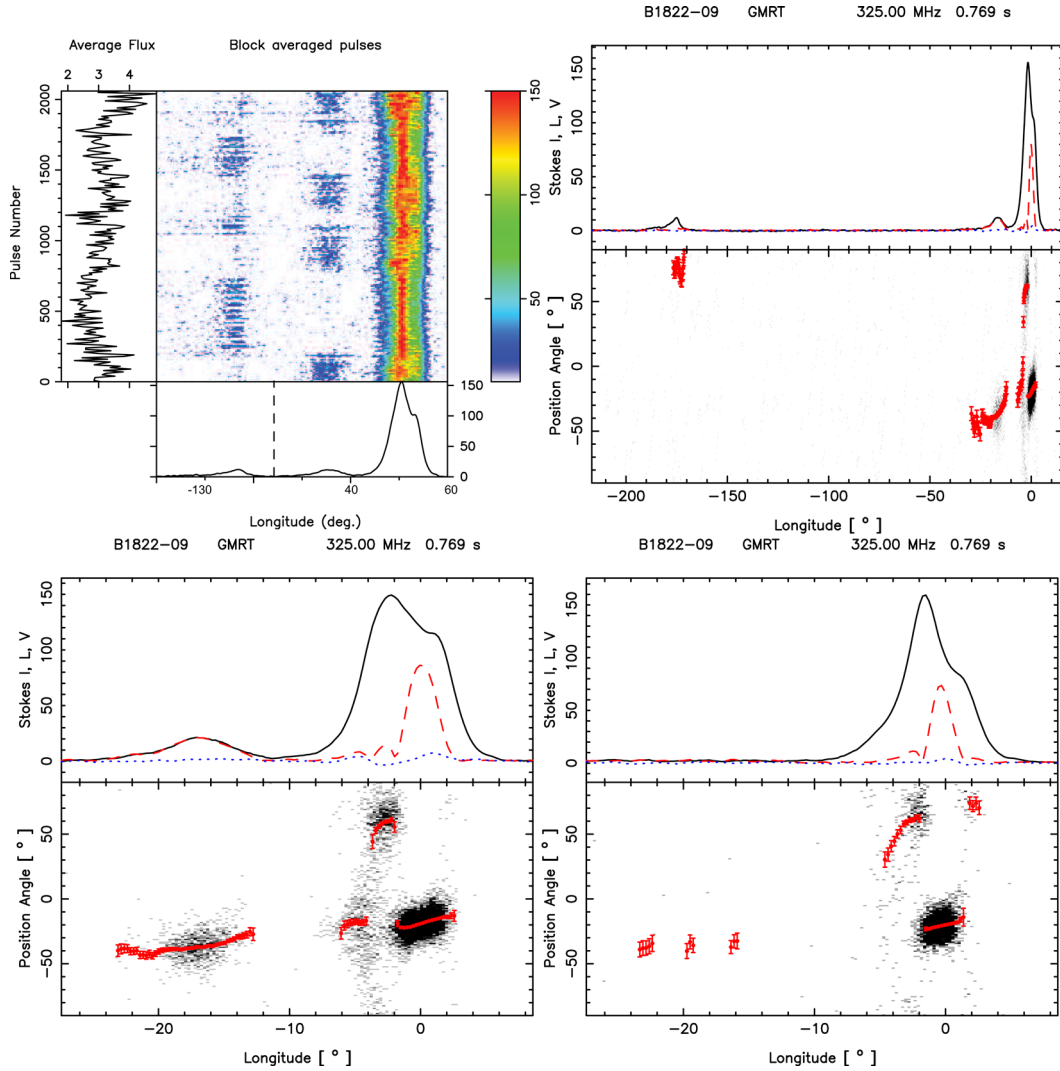


Figure A1. PSR B1822–09 2077-pulse sequence (top left panel) observed with the GMRT at 325 MHz and used for analysis by [BMR10](#); note that a 140° longitude interval is removed at the dashed vertical line. PPA histogram (top right panel) corresponding to this observation. Zoomed in panels showing the B-mode (bottom left panel) and Q-mode PPA histograms, respectively. Note that the PPA histograms below the MP lying between about -10° and $+8^\circ$ longitude are similar for both the B and Q modes.

carried out to find α and β , and the χ^2 contours are shown in Fig. A2. Clearly a wide range of α and β values are consistent with the fits, as the parameters are correlated up to 99 per cent. The left-hand and right-hand panels of Fig. A3 show the RVM solutions for orthogonal and aligned rotator cases, respectively, and these solutions cannot be distinguished (see captions for more details). Hence, RVM fits to the MP PPA traverse cannot constrain the geometry, in particular to distinguish between an orthogonal and aligned rotator.

If the IP could be included in the fits, there would be a possibility to distinguish between the aligned and orthogonal rotator geometries, since the PPA traverses are very different in the IP region as shown in Fig. A4. However, the lack of sufficiently sensitive single-pulse polarization makes this task impossible for the moment.

A2 Geometry using core width

If a core component can be identified in a pulse profile, then Rankin (1990, 1993a,b) has shown that the half-width of the core component (W_c) can be related to α as $\sin(\alpha) = 2.45^\circ P^{-0.5}/W_c$. Furthermore, using the steepest gradient point of the PPA traverse

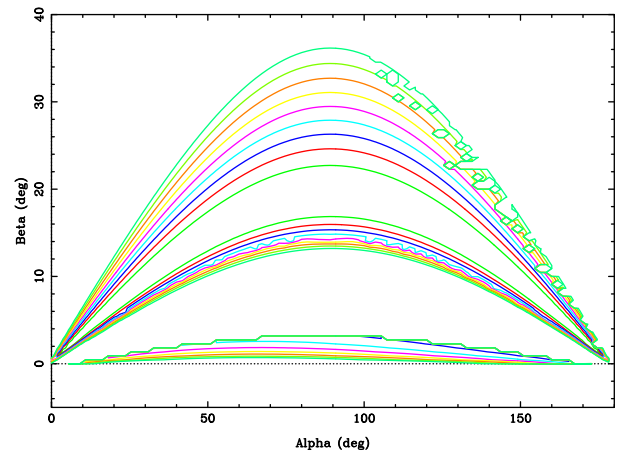


Figure A2. The χ^2 contours are shown of fitting the RVM for various values of α along the x-axis and β along the y-axis. Clearly the χ^2 minimum is unconstrained. The curves represent multiples of the minimum χ^2 as 2 (green), 3 (red), 4 (blue), 5 (cyan), 6 (magenta), 7 (yellow), 8 (orange), 9 (yellow-green) and 10 (cyan-green).

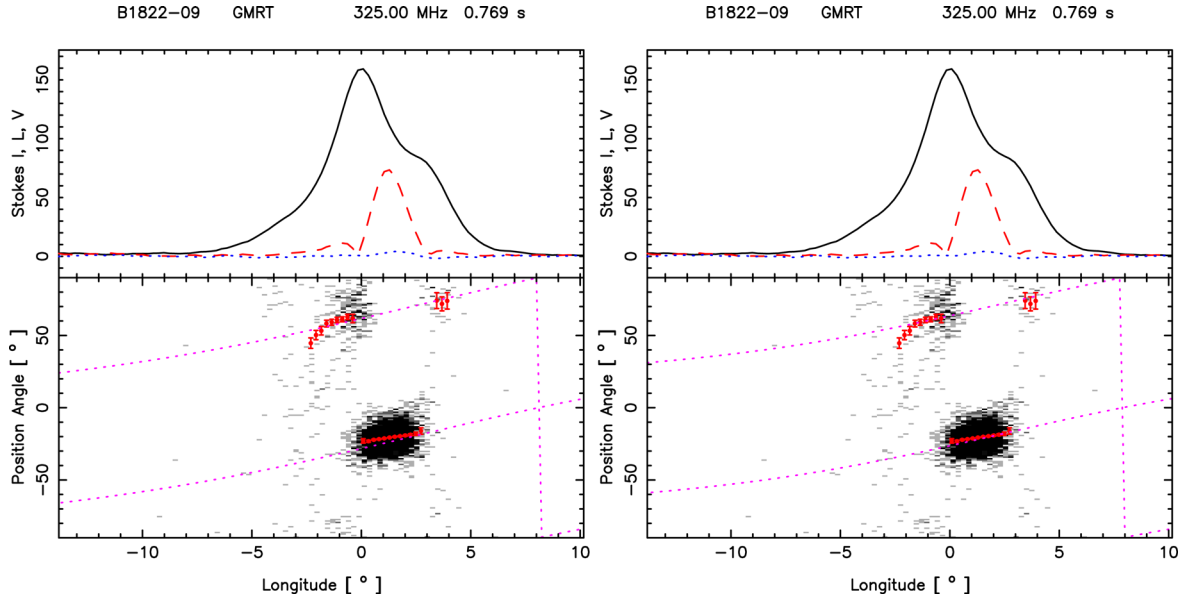


Figure A3. The left-hand and right-hand panels show the RVM fits (as dashed magenta lines) where the left solution corresponds to an approximately orthogonal case with $\alpha = 84^\circ$ and $\beta = 16^\circ$ and the right solution corresponds to an almost aligned case with $\alpha = 7^\circ$ and $\beta = 1^\circ$. These two fits cannot be distinguished.

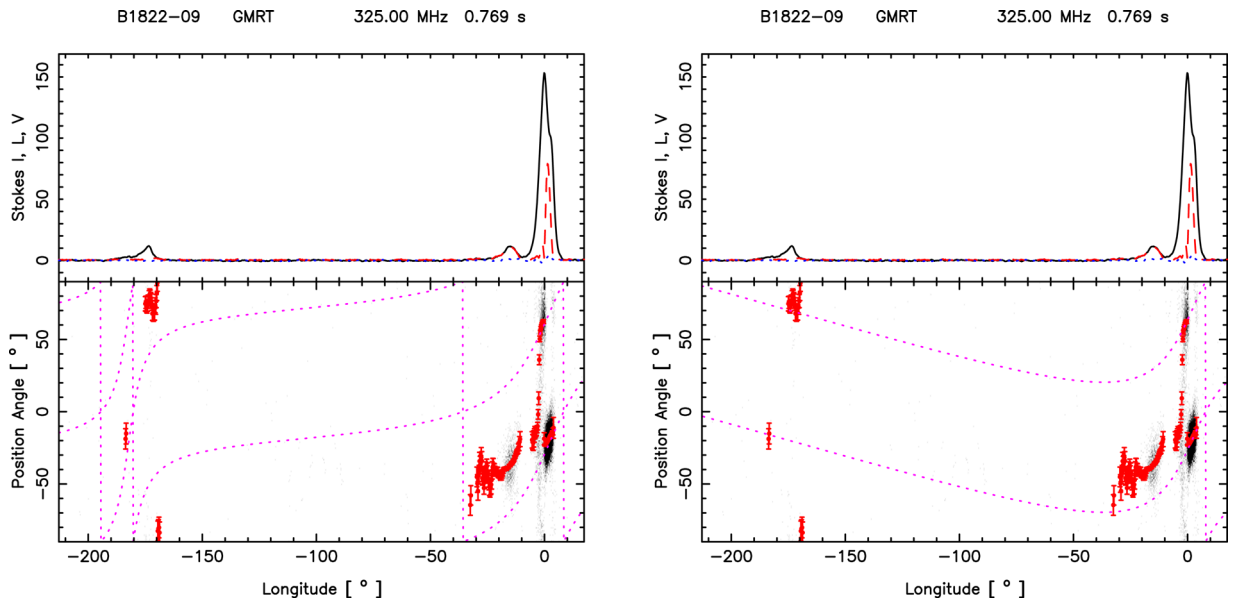


Figure A4. The left-hand panel in this figure shows the full IP–MP RVM for the almost orthogonal rotator case using $\alpha = 84^\circ$ and $\beta = 16^\circ$. The right-hand panel shows the full RVM for an almost aligned case using $\alpha = 7^\circ$ and $\beta = 1^\circ$. Note that in the IP region the two curves show very different behaviour. However, since we cannot distinguish the OPM due to lack of sensitive data, we cannot trace the behaviour of the PPA traverse. The average PPA cannot be used for understanding the RVM.

$R = \sin(\alpha)/\sin(\beta)$, β can be found. Rankin (1993b) classifies the MP of PSR B1822–09 as having a core-cone configuration. Furthermore, her table 5 gives a value of 2.8° for W_c , implying per the above relationship that $\alpha \sim 86^\circ$. Also a value of $R = 50$ (Lyne & Manchester 1988) has been used to get $\beta \sim 1.1^\circ$. From our analysis we confirm that $W_c \sim 2.8^\circ$, however based on our best RVM solutions we find a significantly smaller value for the steepest gradient – i.e. $R \sim 2.4$ giving $\beta \sim 16^\circ$. The unusually large β value is however worrying, since it leads to an unusually large beam radius of about 16° and emission heights of about 1300 km. However, one should realize that for this pulsar the PPA histograms do not constrain R

very well. It hence appears that the lack of a clean description of the RVM for PSR B1822–09 leads to an uncertain geometrical interpretation.

A3 Orthogonal rotator

While the methods for determining α and β largely fail for PSR B1822–09, there is striking evidence that the IP and the MP are separated by almost precisely 180° at 325 MHz (BMR10, Latham et al. 2012) and nearly that over a broad-band (Hankins & Fowler 1986) – though it is important to restudy this separation

on the basis of modern techniques. Furthermore, the narrowness of the MP core component is also strong evidence for an orthogonal alignment, the difficulty of determining β notwithstanding. Most recently, Pilia et al. (2016) show in their fig. B.2 that 350 and 1400 MHz profiles are very well aligned, appearing to be the strongest argument for an orthogonal rotator. Therefore, the existing evidence strongly points to PSR B1822–09 as having an orthogonal rotator geometry. Of course, this orthogonal geometry raises an

urgent question about the origin of the modulational ‘cross-talk’ observed between the pole and interpole of PSR B1822–09 and many more MP-IP pulsars (e.g. Weltevrede, Wright & Stappers 2007; Weltevrede, Wright & Johnston 2012).

This paper has been typeset from a $\text{\TeX}/\text{\LaTeX}$ file prepared by the author.